nature communications

Article

https://doi.org/10.1038/s41467-024-52706-7

# TDP43 aggregation at ER-exit sites impairs ER-to-Golgi transport

Received: 28 April 2024

Accepted: 18 September 2024

Published online: 19 October 2024

Check for updates

Hongyi Wu[1], Loo Chien Wang[2], Belle M. Sow[1], Damien Leow[3], Jin Zhu[1], Kathryn M. Gallo[4,5], Kathleen Wilsbach[4,5], Roshni Gupta[1], Lyle W. Ostrow[4,5], Crystal J. J. Yeo[2,6,7,8,9,10], Radoslaw M. Sobota[2] & Rong Li[1,11]

Protein aggregation plays key roles in age-related degenerative diseases, but how different proteins coalesce to form inclusions that vary in composition, morphology, molecular dynamics and confer physiological consequences is poorly understood. Here we employ a general reporter based on mutant Hsp104 to identify proteins forming aggregates in human cells under common proteotoxic stress. We identify over 300 proteins that form different inclusions containing subsets of aggregating proteins. In particular, TDP43, implicated in Amyotrophic Lateral Sclerosis (ALS), partitions dynamically between two distinct types of aggregates: stress granule and a previously unknown non-dynamic (solid-like) inclusion at the ER exit sites (ERES). TDP43-ERES co-aggregation is induced by diverse proteotoxic stresses and observed in the motor neurons of ALS patients. Such aggregation causes retention of secretory cargos at ERES and therefore delays ER-to-Golgi transport, providing a link between TDP43 aggregation and compromised cellular function in ALS patients.

The intracellular space is crowded with proteins of a few hundred gram per liter concentration[1,2]. To facilitate interaction between partner proteins and prevent unfavorable interaction, a mechanism evolved is the formation of inclusions or aggregates, which assemble functional partners and sequester potentially harmful species such as misfolded proteins[3–6]. In this study, we use the term "aggregate" to broadly refer to distinct foci of proteins visible under optical microscopes, regardless of whether they are functional or dynamic (liquid-like) or cytotoxic or non-dynamic (solid-like).

The aggregation of misfolding-prone proteins is a common hallmark of various neurodegenerative diseases, and different proteins aggregate in different diseases[7–9]. For example, Aβ and τ are the major constituents of aggregates in Alzheimer's disease (AD) whereas α-synuclein aggregates are mainly found in Parkinson's disease (PD). In Amyotrophic Lateral Sclerosis (ALS), various aggregation-prone proteins are implicated, including TAR DNA-binding protein 43 kDa (TDP43), FUS, SOD1, hnRNP A1, UBQLN2, and dipeptide repeats originated from the expanded GGGGCC repeats of C9ORF72[9,10]. In addition to their respective hallmark aggregates, secondary aggregate proteins or concomitant proteinopathies are common to neurodegenerative diseases. For instance, Aβ, τ and α-synuclein aggregates all have been found in ALS-affected brain regions[11,12].

Although many proteins can self-aggregate at high concentration when purified in vitro[13,14], co-aggregation of different proteins greatly expands the repertoire of aggregates formed in cells with varied biochemical and physical properties. For instance, a fraction of

[1]Mechanobiology Institute, National University of Singapore (NUS), Singapore, Singapore. [2]Institute of Molecular and Cell Biology, Agency for Science, Technology and Research (A*STAR), Singapore, Singapore. [3]Department of Anatomy, Yong Loo-Lin School of Medicine, National University of Singapore, Singapore, Singapore. [4]Department of Neurology, School of Medicine, Johns Hopkins University, Baltimore, MD, USA. [5]Department of Neurology, Lewis Katz School of Medicine, Temple University, Philadelphia, PA, USA. [6]National Neuroscience Institute, Singapore, Singapore. [7]Duke-NUS Medical School, Singapore, Singapore. [8]Lee Kong Chian School of Medicine, Nanyang Technological University, Singapore, Singapore. [9]Department of Neurology, Feinberg School of Medicine, Northwestern University, Evanston, IL, USA. [10]School of Medicine, Medical Sciences and Nutrition, University of Aberdeen, Aberdeen, Scotland, UK. [11]Department of Biological Sciences, National University of Singapore, Singapore, Singapore. e-mail: mbihead@nus.edu.sg

cytoplasmic TDP43 co-aggregates with RNAs, ribosomal proteins and other RNA-binding proteins in stress granules (SGs) and remains soluble (liquid-like) until prolonged stress induces a liquid-to-solid phase transition[15–17]. However, when these SGs also contained the nucleoporin NUP62, TDP43 turns insoluble[18,19]. Upon proteasome inhibition, many proteins such as CFTR and PS1$^{A246E}$ accumulate ubiquitinated species and aggregate near the nucleus and microtubule organization center (MTOC) to form a single non-dynamic (solid-like) inclusion termed aggresome[20,21]. At a similar subcellular location, SOD1$^{G93A}$ co-aggregates with either VHL in a dynamic (liquid-like) inclusion termed JUxta Nuclear Quality control compartment (JUNQ), or with polyQ Htt into a distinct non-dynamic (solid-like) inclusion termed Insoluble Protein Deposit (IPOD)[22,23].

The diversity of protein aggregates poses a great challenge for comprehending their physiological consequences, especially given that different aggregates may form at either early or late disease stage and exert cytoprotection or toxicity through distinct mechanisms[15–17]. Clinically, aggregates are often categorized by their appearance in patient samples. For example, TDP43 aggregates found in ALS can be classified into skein-like, round, dot-like, linear wisps, and diffuse punctate cytoplasmic staining (DPCS), and it was proposed that DCPS is an early-stage pathology of ALS[10,24]. However, much remains to be understood about how aggregate morphology relates to the aggregate's composition, subcellular distribution, biophysical properties, and pathophysiological impacts.

Although many studies have investigated the aggregation of specific disease-associated proteins using protein-specific labels, such as antibodies and fluorescent protein (FP) tags, to observe the formation of diverse protein inclusions requires more general markers that broadly label aggregates of misfolded proteins. In yeast, observation of misfolded protein aggregation often employed Hsp104 tagged with an FP[25–28]. Hsp104 is a molecular chaperone, a protein disaggregase that recognizes misfolded proteins via interaction with Hsp70/40 chaperones and binding of its N-terminal domain (NTD) to the hydrophobic stretches exposed by misfolded substrates[29,30]. Hsp104 disassembles aggregates by forming hexameric ring-like complexes, through which misfolded proteins are threaded to be disentangled[31,32]. In yeast, Hsp104-FP foci indicate the locations of aggregates. By using this method, our previous study showed that Hsp104-labeled aggregates are formed on the cytoplasmic surface of ER and mostly remain associated with the ER and mitochondria during their lifetime[33]. The human proteome does not appear to contain an Hsp104 ortholog[34,35], but potentiated Hsp104 variants can disaggregate human proteins such as TDP43 and FUS in vitro or expressed in yeast[36,37], indicating that Hsp104 is capable of recognizing misfolded proteins of human origin.

In this study, we repurposed a mutant Hsp104 that stably binds misfolded proteins as a broad-spectrum reporter/marker for protein inclusions in human cells. Using this reporter, we profiled the protein composition of stress-induced aggregates purified from human cells and uncovered diverse types of aggregates with different but overlapping protein compositions. We observed that TDP43 co-aggregates with SEC16A and the COPII protein complex in ER-exit sites (ERES) to form non-dynamic (solid-like) inclusions, which morphologically resembles the diffuse punctate cytoplasmic staining (DPCS) of TDP43, the proposed early-stage pathology of ALS. Further investigation showed that TDP43-ERES co-aggregation impairs ER-to-Golgi transport, suggesting a mechanism for TDP43 to cause cellular dysfunction potentially associated with ALS.

## Results

### Identification of aggregation-prone proteins in human cells using an Hsp104-based reporter

To visualize various types of stress-induced aggregates, we explored the use of FP-tagged Hsp104 as a general marker of protein aggregates in human cells. We introduced the Double Walker B (DWB) mutations (E285Q and E687Q), which fall in the Walker B motifs of both nucleotide-binding domains (NBD1 and NBD2) of Hsp104, to disrupt ATP hydrolysis by Hsp104 required for disaggregation. Because we were concerned that WT Hsp104 expressed in mammalian cells would disassemble aggregates, Hsp104$^{DWB}$ was used as it binds but does not disassemble aggregates[36–38] (Supplementary Fig. 1a, b). To validate its effectiveness as an aggregate marker in human cells, we co-transfected Hsp104$^{DWB}$-mEGFP with aggregation-prone proteins TDP43$^{Q331K}$-mCherry or SOD1$^{G93A}$-mCherry into human RPE-1, a non-transformed cell line that maintains a near-diploid karyotype[39]. Heat stress (42 °C), which occurs under certain pathological conditions and destabilizes protein folding[40,41], was used to exacerbate protein aggregation. Like previous studies, we stressed the cells for a duration of 12-16 hr to allow misfolded proteins to accumulate[20,42–44]. 3D confocal imaging revealed that Hsp104$^{DWB}$ was enriched in most aggregates of TDP43$^{Q331K}$ or SOD1$^{G93A}$, demonstrating that Hsp104$^{DWB}$ recognized aggregates of different proteins (Fig. 1a, b). However, over 50% Hsp104$^{DWB}$ aggregates did not colocalize with TDP43$^{Q331K}$ or SOD1$^{G93A}$ aggregates and likely represent aggregates of endogenous proteins (Fig. 1a, c).

We subsequently utilized Hsp104$^{DWB}$-mEGFP to observe aggregates of endogenous proteins induced by proteotoxic stress. In untreated or DMSO mock-treated RPE-1 cells, the average number of Hsp104$^{DWB}$ aggregates per cell was close to 0. In contrast, many aggregates labeled with Hsp104$^{DWB}$-mEGFP emerged in cells under heat stress or treatment with MG132 (Fig. 1d, e), inhibitor of aspartyl proteases and cysteine proteases also found in proteasomes, another condition often used to induce protein aggregation[42,43]. Aggregates enriched for Hsp104$^{DWB}$-mEGFP-FLAG were also observed in another human cell line, HEK293T, under heat stress (Supplementary Fig. 1c). As a control, mEGFP-FLAG alone did not aggregate under the same condition (Supplementary Fig. 1c).

To identify endogenous proteins harbored by stress-induced aggregates, we used Hsp104$^{DWB}$-mEGFP-FLAG as a bait for affinity-purification. This reporter was transfected into human HEK293T cell line, which expresses most proteins found in different tissues and has been widely used for protein purification[45–47]. Lysates of heat stressed HEK293T cells were first fractionated by sucrose gradient centrifugation to separate aggregates from soluble proteins (Supplementary Fig. 1d III-V). Immunoprecipitation was then performed with anti-FLAG tag resin (Supplementary Fig. 1d VI and VII) to further separate aggregates labeled with Hsp104$^{DWB}$-mEGFP-FLAG from other macromolecular assemblies and organelles. As a control, cells transfected with Hsp104$^{DWB}$-mEGFP without FLAG tag were subjected to the same workflow. The precipitated proteins were analyzed by liquid chromatography (LC) and quantitative mass-spectrometry (MS) (Supplementary Fig. 1d VIII).

337 proteins were found to be enriched in the immunoprecipitate by more than 8.5-fold when compared with the control (Supplementary Fig. 1e, f, Supplementary Data 1). Gene Ontology (GO) analysis revealed that chaperones and other proteins involved in folding and stress response (e.g. Hsp70/40/90 families, chaperonin and VCP) were the top-enriched categories, as expected (Supplementary Fig. 1g, h, Supplementary Data 1). Moreover, proteins involved in RNA metabolism and translation (e.g. TDP43, RNA helicases and translational initiation factors) were overrepresented (Supplementary Fig. 1g, h, Supplementary Data 1), probably because the prion-like domains present in many RNA-binding proteins promote misfolding and aggregation[48,49]. Among the top hits there were also nucleoporins, including NUP214, which contains phenylalanine-glycine (FG) repeats, and its close interaction partner NUP88 (Supplementary Fig. 1g, h, Supplementary Data 1)[50–52]. Lastly, in support of the recent findings that macromolecular condensates accumulate misfolded proteins[16,17,53], many aggregate proteins found are components of SGs or nucleoli (e.g. G3BP1 and RPA40), or contain significant disordered

https://doi.org/10.1038/s41467-024-52706-7

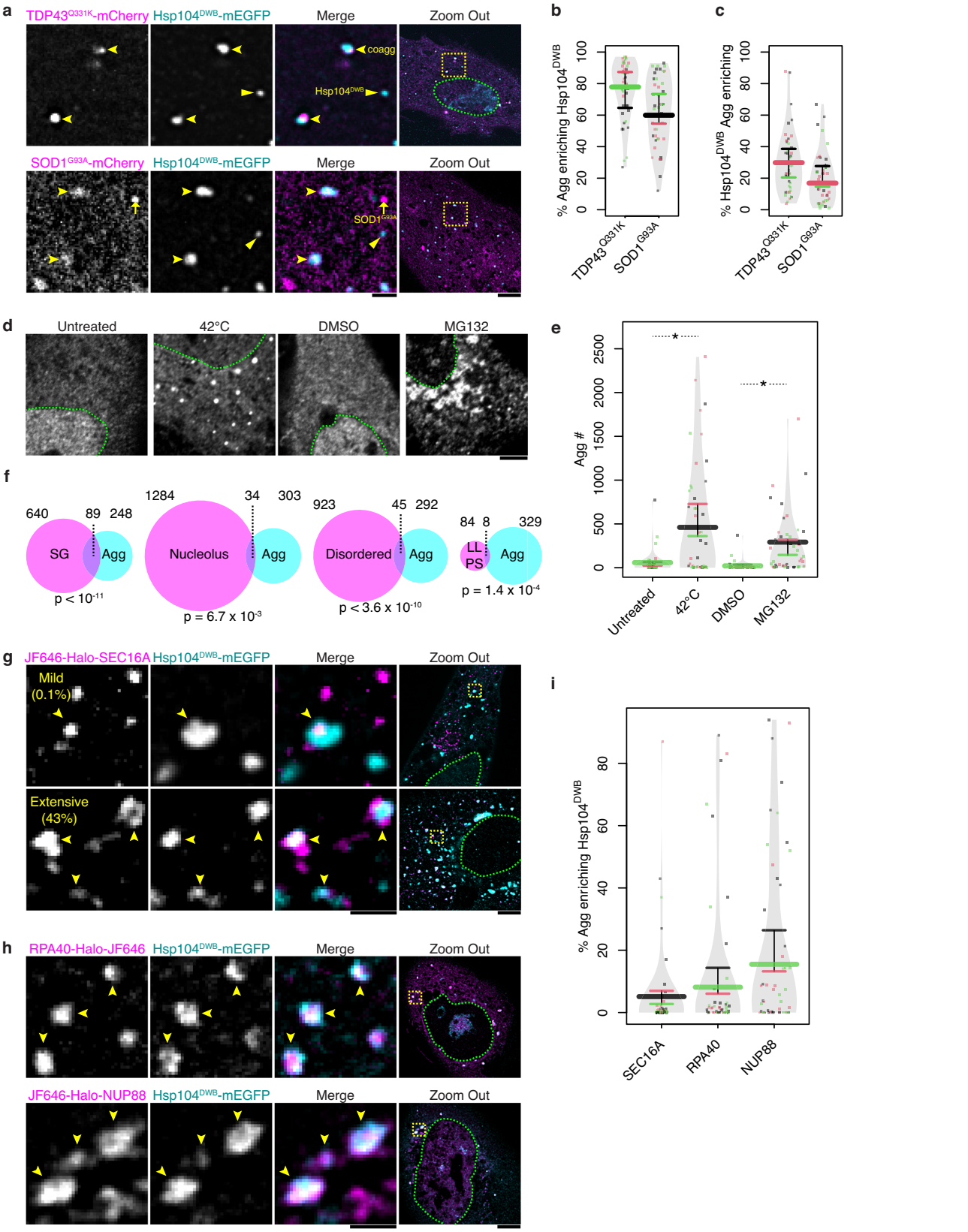


regions, or have been reported to undergo liquid-liquid phase separation (LLPS) in vitro (Fig. 1f, Supplementary Fig. 1h, Supplementary Data 1).

Apart from some well-known aggregation-prone proteins, such as TDP43 and the SG component G3BP1, we identified many proteins that had not been previously reported to participate in misfolded-protein aggregates. Three candidate proteins that represent different cellular functions/components, namely SEC16A, RPA40 and NUP88, were selected for validation by imaging. SEC16A is a cytoplasmic protein that defines ER-exit sites (ERES) by forming dynamic (liquid-like) inclusions at certain locations of the ER surface, and recruits COPII complexes to drive vesicle budding to transport cargos towards the

**Fig. 1 | Hsp104$^{DWB}$ enables visualization of aggregates and identification of aggregate proteins in human cells. a** Representative images showing the colocalization between Hsp104$^{DWB}$ and aggregates formed by TDP43$^{Q331K}$ or SOD1$^{G93A}$ after RPE-1 cells were incubated at 42 °C for 12–16 hr. Representative slices of confocal z-stacks are displayed. Arrowheads indicate Hsp104$^{DWB}$-labeled TDP43$^{Q331K}$ or SOD1$^{G93A}$ aggregates (i.e. co-aggregate or coagg); arrows indicate SOD1$^{G93A}$ aggregates without Hsp104$^{DWB}$; triangles indicate Hsp104$^{DWB}$ aggregates without TDP43$^{Q331K}$ or SOD1$^{G93A}$. The region displayed in individual channels and Merge views is indicated by the yellow box in "Zoom Out", and green dashes demarcate the nucleus. Scale bars except in "Zoom Out" represent 1 μm, and represent 5 μm in "Zoom Out". **b** Quantification of the experiments as in (**a**) showing the percentage (% by number) of TDP43$^{Q331K}$ or SOD1$^{G93A}$ aggregates (Aggs) marked by Hsp104$^{DWB}$. $n = 45$ cells examined over 3 independent experiments. The values of individual cells are plotted as dots, and the mean values of cells in the same experiment as horizontal segments, the median of which is elongated and thickened. Different colors denote different experiments. **c** Quantification of the experiments as in (a) showing the percentage of Hsp104$^{DWB}$ aggregates that enriched for TDP43$^{Q331K}$ or SOD1$^{G93A}$. $n = 45$ cells examined over 3 independent experiments. The values of individual cells are plotted as dots, and the mean values of cells in the same experiment as horizontal segments, the median of which is elongated and thickened. Different colors denote different experiments. **d** Representative images showing stress-induced aggregates of endogenous proteins labeled by Hsp104$^{DWB}$-mEGFP in cells without or with heat stress (42 °C), or treated with DMSO or 10 μM MG132 for 12–16 hr. The scale bar represents 1 μm. **e** Quantification of the experiments as in (**d**) comparing the numbers (#) of aggregates in each cell under different conditions. $n = 45$ cells examined over 3 independent experiments. The values of individual cells are plotted as dots, and the mean values of cells in the same experiment as horizontal segments, the median of which is elongated and thickened. Different colors denote different experiments. Asterisks (*) indicate p-value ≤ 0.05 in two-sided t-tests between experimental means. **f** Venn diagrams showing the overlaps between proteins identified in Hsp104$^{DWB}$-bound aggregates and the protein components of stress granule (SG) and nucleolus and proteins that contain significant disordered regions or undergo in vitro liquid-liquid phase separation (LLPS). P-values of hypergeometric tests are displayed. **g** Representative images of aggregates containing SEC16A and their colocalization with Hsp104$^{DWB}$. Examples for SEC16A inclusions enriching Hsp104$^{DWB}$ mildly (<10%) and more extensively (≥ 10%) are shown. Arrowheads indicate SEC16A aggregates recognized by Hsp104$^{DWB}$. Scale bars except in "Zoom Out" represent 1 μm, and represent 5 μm in "Zoom Out". Experiments hereafter were performed in RPE-1 cells stressed at 42 °C for 12–16 hr unless indicated otherwise. **h** Representative images of the aggregates formed by RPA40 and NUP88 and their colocalization with Hsp104$^{DWB}$. Scale bars except in "Zoom Out" represent 1 μm, and represent 5 μm in "Zoom Out". **i** Quantification of the experiments as in (**g** and **h**) showing the percentage of SEC16A, RPA40 and NUP88 aggregates labeled by Hsp104$^{DWB}$ in each cell. $n = 45$ cells examined over 3 independent experiments. The values of individual cells are plotted as dots, and the mean values of cells in the same experiment as horizontal segments, the median of which is elongated and thickened. Different colors denote different experiments.

Golgi[54–57]. RPA40, also known as POLR1C, is a DNA-dependent RNA polymerase found in the nucleoplasm and the fibrillar centers of nucleoli[53]. NUP88 is a subunit of the cytoplasmic filaments of the nuclear pore complex (NPC)[58]. The abundance of these three proteins in aggregates was medium among the identified proteins (Supplementary Fig. 1e, f). Each of these proteins was fused with a HaloTag (Halo) and co-transfected with Hsp104$^{DWB}$-mEGFP into cultured cells for confocal imaging.

We first validated in HEK293T cell line that SEC16A, RPA40 and NUP88 were present in Hsp104-labeled aggregates after heat stress (Supplementary Fig. 2a, b). For better observation of subcellular localization, we expressed these proteins in RPE-1 cells, which are bigger in size. Under heat stress, all three proteins formed aggregates, some though not all of which were marked by Hsp104$^{DWB}$-mEGFP (Fig. 1g–i). Unlike the aggresome, JUNQ or IPOD, which are aggregates found in the vicinity of the nucleus and MTOC[20,22,23], Hsp104$^{DWB}$-labeled aggregates of SEC16A, RPA40 or NUP88 were found throughout the cytoplasm (Fig. 1g–i). Notably, cells displayed marked heterogeneity in the percentage of aggregates labeled by Hsp104$^{DWB}$. For example, the majority of cells contained no or <10% SEC16A inclusions recognized by Hsp104$^{DWB}$, whereas a small fraction of cells displayed much more extensive aggregation of misfolded proteins (>10% SEC16A inclusions with Hsp104$^{DWB}$) (Fig. 1g, i).

## Differential preference in protein co-aggregation

We next investigated if the proteins validated above formed the same or different aggregates by analyzing the pairwise co-aggregation of these proteins under heat stress. We co-transfected plasmids expressing each pair of the aggregation-prone proteins into RPE-1 cells to examine their propensity to form co-aggregates (coaggs). It turned out that not all proteins aggregated into the same inclusions, but each coalesced with its selective partners at different levels of efficiency (Fig. 2a–h, Supplementary Fig. 3a). For example, TDP43 co-aggregated with G3BP1, SEC16A and NUP88 with sequentially decreasing levels but did not aggregate with RPA40 (Fig. 2a–d, h). Again, we observed heterogeneity in the degree of coaggs formation among cells. For example, the majority of cells co-expressing TDP43-mNG and Halo-SEC16A contained no or low numbers of TDP43/SEC16A coaggs, whereas some cells exhibited much more extensive co-aggregation (Fig. 2b). Such heterogeneity was partially attributed to the different expression levels of TDP43 and SEC16A after transient transfection, as there was weak positive correlation between co-aggregation levels and the integrated intensities of TDP43 and SEC16A (Supplementary Fig. 2c, d). Nevertheless, TDP43/SEC16A co-aggregation was not solely determined by expression levels, as some cells with below-median expression levels formed coaggs and vice versa (Supplementary Fig. 2c, d).

Notably, G3BP1, SEC16A and NUP88 rarely co-aggregated with each other even though they all showed some degree of co-aggregation with TDP43 (Fig. 2e–h). We further confirmed that the coaggs of TDP43/G3BP1 (i.e. TDP43-containing SGs) and TDP43/SEC16A are orthogonal types of aggregates by simultaneously labeling TDP43, G3BP1 and SEC16A with different fluorescent tags. Even though TDP43/G3BP1 and TDP43/SEC16A coaggs could co-exist in the same cells and some appeared adjacent to each other, they did not fuse or colocalize (Fig. 2i). Importantly, RNA fluorescence in situ hybridization (FISH) revealed that TDP43/G3BP1 coaggs contained abundant polyadenine (polyA) RNAs, as previously reported[59], whereas TDP43/SEC16A coaggs were devoid of polyA RNA (Supplementary Fig. 4a).

To examine whether TDP43 and SEC16A directly interact in co-aggregates, we employed a system of dimerization-dependent FP (ddFP) consisting of a pair of nonfluorescent FP-derived monomers that can stably fluoresce only when two proteins tagged by each part of the ddFP heterodimerize[60]. When TDP43 and SEC16A were respectively tagged with mEGFP-ddRFP-B and ddRFP-A-Halo, TDP43/SEC16A coaggs emitted ddRFP fluorescence (Supplementary Fig. 3b). As a control, G3BP1 tagged with ddRFP-B-EGFP was coexpressed with ddRFP-A-Halo-SEC16A. Although some SEC16A aggregates and G3BP1 aggregates (i.e. SGs) appeared adjacent to each other, no ddRFP fluorescence was detected (Supplementary Fig. 3b).

Timelapse imaging revealed that TDP43 partitions dynamically between SGs and TDP43/SEC16A coaggs. In about half of the cells that formed SGs under heat stress, SGs were observed to undergo spontaneous dissolution to below 10% of the initial volume. In these cells, TDP43/SEC16A coaggs gradually emerged as SGs were disappearing (Supplementary Fig. 4d, e, Supplementary Movie 1), and exhibited a significantly higher increase of TDP43 intensity in coaggs with SEC16A when compared with cells that maintained SGs (Supplementary Fig. 4f). We confirmed that such dynamic TDP43 partition was not due to G3BP1 overexpression in the above experiment, as the same phenomenon was observed in cells where the endogenous G3BP1 was tagged in-frame with mScarlet-I through CRISPR/Cas-mediated genome editing without ectopic G3BP1 expression (Supplementary

https://doi.org/10.1038/s41467-024-52706-7

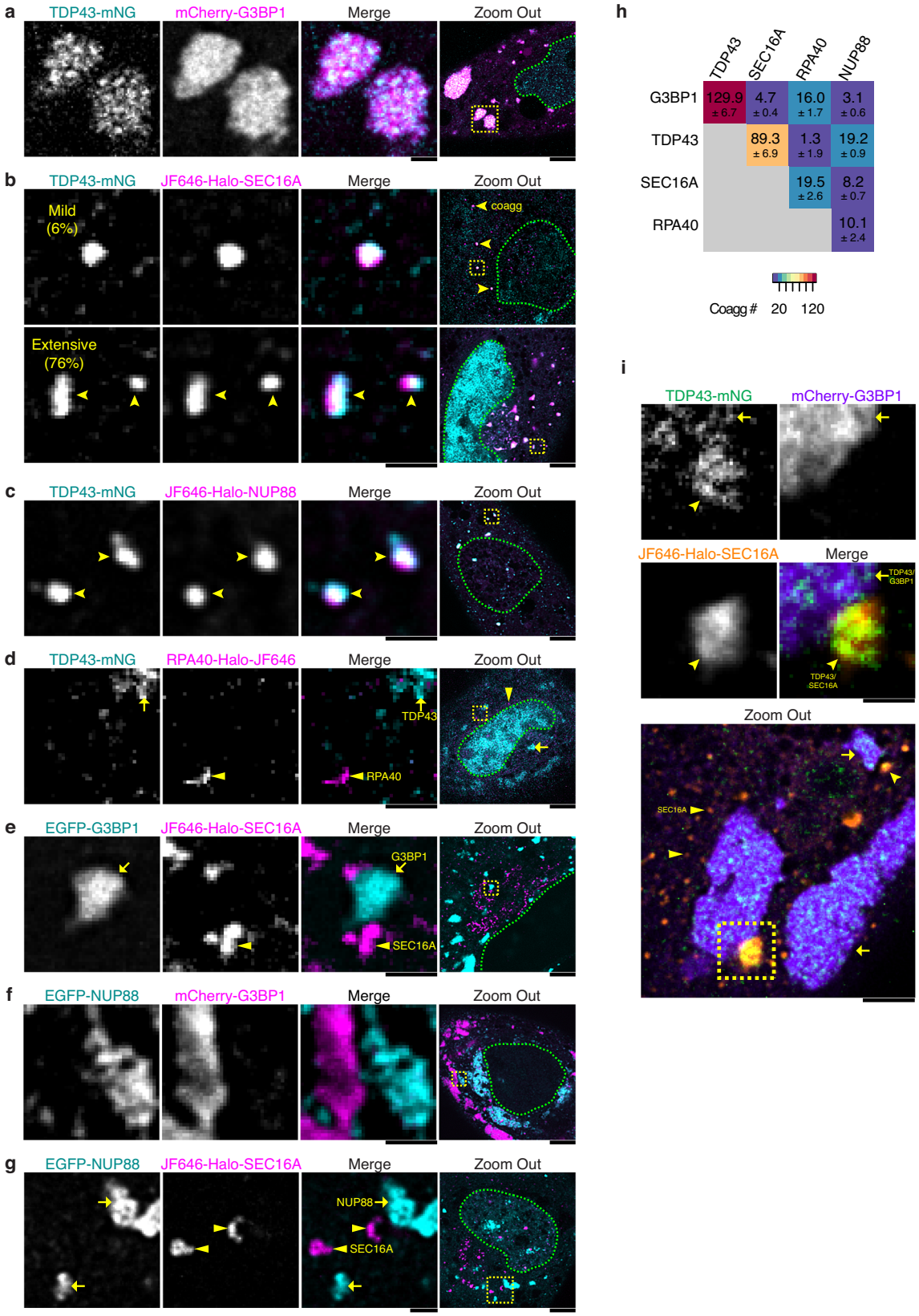


Fig. 4g). In addition, to test if the partition of TDP43 can also be modulated by the level of SGs, we overexpressed G3BP1 or used RNA interference (RNAi) to inhibit G3BP1/2 expression, which respectively stimulated or suppressed SG assembly (Supplementary Fig. 4h, i)[61,62]. Correspondingly, the percentage of SEC16A inclusions accumulating TDP43 was respectively reduced or increased (Supplementary Fig. 4j). Furthermore, TDP43$^{5FL}$, an RNA-binding-deficient mutant with reduced recruitment to SGs[15], displayed increased co-aggregation with SEC16A when compared with wild-type (WT) TDP43 (Supplementary Fig. 4b, c). Together, these results suggest that TDP43 co-aggregation with SEC16A is modulated by the capability of SGs to recruit TDP43.

**Fig. 2 | Selective co-aggregation among aggregate-forming proteins.** **a** Representative images showing that, when co-transfected into RPE-1 cells, TDP43 co-aggregated with G3BP1 in stress granule (SG). In "Zoom out", the yellow box indicates the region shown in zoom-in views, and green dashes demarcate the nucleus. Scale bars except in "Zoom Out" represent 1 μm, and represent 5 μm in "Zoom Out". **b** Representative images for SEC16A inclusions enriching TDP43 mildly (<10%) and more extensively (≥ 10%) are shown. Arrowheads: co-aggregates (coaggs). Scale bars except in "Zoom Out" represent 1 μm, and represent 5 μm in "Zoom Out". **c** Representative images showing TDP43 co-aggregation with NUP88 in the cytoplasm. Scale bars except in "Zoom Out" represent 1 μm, and represent 5 μm in "Zoom Out". **d** Representative images showing that TDP43 rarely co-aggregated with RPA40. Arrows: TDP43 aggregates; triangles: RPA40 aggregates. Scale bars except in "Zoom Out" represent 1 μm, and represent 5 μm in "Zoom Out". **e** Representative images showing that G3BP1 rarely co-aggregated with SEC16A. Arrows: G3BP1 aggregates; triangles: SEC16A aggregates. Scale bars except in "Zoom Out" represent 1 μm, and represent 5 μm in "Zoom Out". **f** Representative images showing that G3BP1 rarely co-aggregated with NUP88. Scale bars except in "Zoom Out" represent 1 μm, and represent 5 μm in "Zoom Out". **g** Representative images showing that NUP88 rarely co-aggregated with SEC16A. Arrows: NUP88 aggregates; triangles: SEC16A aggregates. Scale bars except in "Zoom Out" represent 1 μm, and represent 5 μm in "Zoom Out". **h** Co-aggregation matrix of TDP43, G3BP1 and newly identified aggregation-prone proteins SEC16A, RPA40 and NUP88. The number in each colored square is the mean number of coaggs per cell ± standard deviation (s.d.) derived from analysis of the experiments as in (**a**–**g**) and Supplementary Fig. 3a. $n = 45$ cells examined over 3 independent experiments. **i** TDP43/SEC16A, TDP43/G3BP1 coaggs (i.e. TDP43-containing SGs) and SEC16A inclusions without TDP43 in the same cell, which are marked by arrowheads, arrows and triangles, respectively. Representative images from 3 independent experiments are shown. Scale bars except in "Zoom Out" represent 1 μm, and represent 5 μm in "Zoom Out".

## TDP43/SEC16A coaggs are formed by TDP43 coalescence with ERES under proteotoxic stress

Whereas TDP43/G3BP1 and TDP43/NUP88 coaggs had been reported previously[15,19], TDP43/SEC16A coaggs represents a new class of TDP43-containing aggregates, which we further investigated. Immunofluorescence staining revealed the co-aggregation of endogenous untagged TDP43 and SEC16A under heat stress or combined with MG132 (Supplementary Fig. 3d, e). TDP43/SEC16A coaggs could also be observed in different cell types including HEK293T (Supplementary Fig. 3f) and motor neurons (elaborated further below). Apart from heating, TDP43/SEC16A coaggs could be induced by other proteotoxic stresses such as treatment with MG132 or the autophagy inhibitor Bafilomycin A1 (Baf) (Fig. 3a, b). Acute treatment by a sublethal concentration (0.5 mM) of sodium arsenite (As) for 1 hr induced TDP43-containing SGs as reported previously (Supplementary Fig. 5a)[15,63,64], although TDP43 level in As-induced SGs was lower than in heat-induced SGs (Supplementary Fig. 5a, b, Fig. 2a). Moreover, the acute arsenite treatment did not induce TDP43/SEC16A coaggs (Fig. 3a, b). Recently, it was reported that in certain types of cells treated with elevated concentration of sodium chloride (NaCl) for 4 hr, ERES become enlarged dynamic (liquid-like) condensates, termed Sec bodies (SBs)[65,66], but whether SBs contain TDP43 was unknown. We thus treated RPE-1 cells with the same stress, but it did not induce TDP43/SEC16A co-aggregation (Fig. 3a, b), indicating that TDP43/SEC16A coaggs were distinct from SBs.

To observe how TDP43/SEC16A coaggs initiate under proteotoxic stress, we performed timelapse imaging of cells subjected to heat stress at 42 °C. Rather than co-assembly with soluble SEC16A to produce coaggs de novo, TDP43 gradually aggregated in pre-existing SEC16A inclusions (Supplementary Fig. 5c, Fig. 3c, d, Supplementary Movie 2). These SEC16A inclusions often became enlarged or clumped as TDP43 accumulated (Fig. 3c, Supplementary Fig. 5d) and this can be observed under various stress conditions (Fig. 3a). The average size of TDP43/SEC16A coaggs, as estimated by structured illumination microscopy (SIM), was ~0.25 $\mu m^3$, substantially larger than that of SEC16A inclusions without TDP43 ( ~0.06 $\mu m^3$) but smaller than SGs containing TDP43 ( ~2.5 $\mu m^3$) (Supplementary Fig. 5e). Nonetheless, ~20% TDP43/SEC16A coaggs had similar size as SEC16A inclusions without TDP43, indicating that size alone was insufficient to distinguish between them (Supplementary Fig. 5f).

We next examined whether TDP43/SEC16A coaggs contained COPII protein complex, which consists of SEC23/SEC24 subcomplex as the inner layer and SEC13/SEC31 as the outer layer, and are recruited to SEC16A inclusions to form mature ERES (Supplementary Fig. 5c)[55,67,68]. Notably, not all SEC16A inclusions colocalized with SEC24C or SEC31, but almost all TDP43/SEC16A coaggs contained both COPII proteins and the percent COPII recruitment was much higher than that of SEC16A inclusions without TDP43 (Fig. 3e–g), indicating that TDP43/SEC16A coaggs originated from mature ERES. In cells that contained TDP43/SEC16A coaggs, the volume percentage [v/v] of (mature) ERES (defined as SEC16A/SEC31A foci) that enriched TDP43 was ~30% on average (Fig. 3h). Interestingly, in these cells, SEC16A inclusions without TDP43 exhibited further reduced levels of COPII recruitment compared to those in cells free of TDP43/SEC16A coaggs (Fig. 3f, g), suggesting that TDP43/SEC16A coaggs sequestrate COPII subunits away from other SEC16A inclusions. Further supporting that TDP43/SEC16A coaggs resulted from TDP43 aggregation with ERES, timelapse imaging revealed that TDP43/SEC16A coaggs remained associated with the ER like other SEC16A inclusions (Fig. 3i, j, Supplementary Movie 3). Therefore, we hereafter refer to TDP43/SEC16A coaggs as "TDP43-ERES", and ERES without TDP43 aggregation as "ordinary ERES".

TDP43 proteins that accumulate in ALS-affected neurons are often subject to phosphorylation (commonly at Ser409 and Ser 410)[24,69,70], although it has also been suggested that hyperphosphorylation suppresses aggregation[71]. It remains unclear which forms of TDP43 cause cellular dysfunction and death and which forms are a result of cellular malfunction[72,73]. We examined whether TDP43 in co-aggregation with ERES was phosphorylated at Ser409 by using an antibody specific for this species ($TDP43^{pSer409}$) and found that $TDP43^{pSer409}$ was not enriched in TDP43-ERES but rather was in SGs (Supplementary Fig. 5g, h). In addition, ubiquitinated TDP43 has served as a clinical marker for ALS, although the non-ubiquitinated isoform was also shown to be enriched in aggregates[10,24]. By immunostaining against ubiquitin (Ub), we found that TDP43-ERES were not enriched for ubiquitin, regardless of whether MG132 was applied to prevent degradation of ubiquitinated proteins (Supplementary Fig. 5i, j). By contrast, ubiquitin was observed to enrich in SGs and the level increased dramatically after MG132 treatment (Supplementary Fig. 5i, j).

Because TDP43 is an RNA-binding protein but TDP43-ERES did not contain polyA RNA (Supplementary Fig. 4a), we suspected that newly synthesized or unfolded TDP43 were enriched in ERES. To test this, we employed a system of Halo-tagged TDP43 and different HaloTag ligand dyes to differentiate between pre-existing (mature) versus newly synthesized (new) TDP43 (Supplementary Fig. 6a). To facilitate this analysis, we used MG132 to inhibit the proteasomal degradation of soluble TDP43[74]. Although both the mature and new pools of TDP43 aggregated in ERES (Supplementary Fig. 6b, Supplementary Movie 4), the ratio between the new and mature TDP43 in ERES, normalized to the new/mature ratio of TDP43 in the whole cell, was always greater than one (Supplementary Fig. 6c, d), indicating that newly synthesized rather than mature TDP43 was the favored substrate for aggregation in ERES. Such selectivity for nascent TDP43 was not attributed to different dye properties, as the preference was not abolished by switching the use of dyes (Supplementary Fig. 6e). Interestingly, the normalized new/mature ratio gradually decreased during the lifetime of TDP43-

https://doi.org/10.1038/s41467-024-52706-7

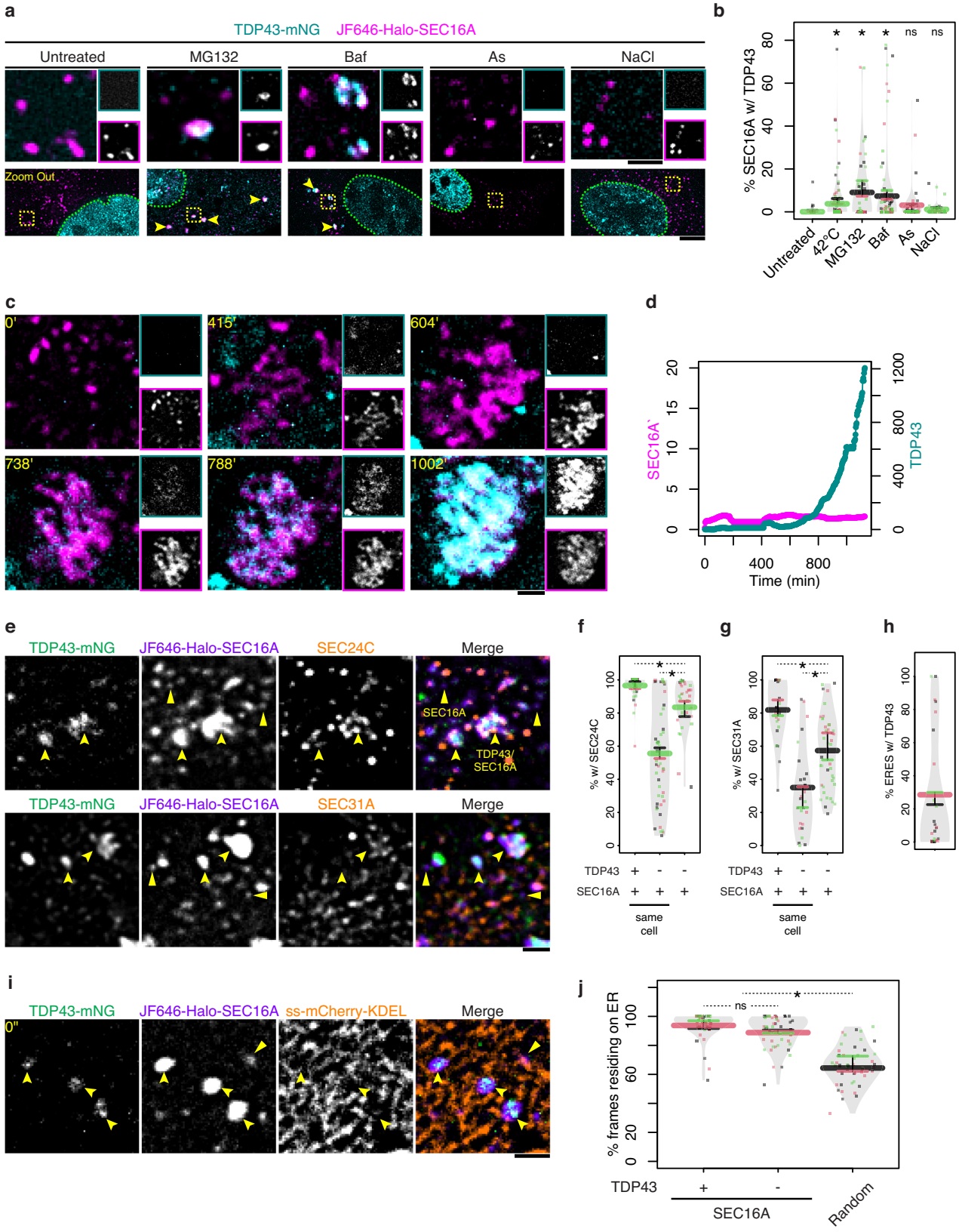


ERES (Supplementary Fig. 6c, d), suggesting that nascent TDP43 formed the seed for aggregation, to which pre-existing TDP43 was added during aggregate growth. In support of this possibility, cycloheximide (CHX), an inhibitor of protein synthesis, strongly suppressed TDP43 aggregation in ERES (Supplementary Fig. 6f, g). In ALS-affected neurons, TDP43 aggregates contain not only full length TDP43 but also truncated variants, such as 35 kDa and 25 kDa C-terminal (C′)-fragments[75,76]. Notably, Halo-TDP43 used in pulse-chase experiment was tagged at the N terminus (N′) whereas TDP43-mNG used in previous experiments was tagged at the C terminus, but both formed TDP43-ERES, suggesting that co-aggregation with ERES did not require N′- or C′-truncation.

**Fig. 3 | Proteotoxic stress induces TDP43 aggregation with preformed ERES.** **a** Representative images showing TDP43/SEC16A coaggs in cells treated with 10 μM MG132 or 100 nM Bafilomycin A1 (Baf) for 12-16 hr. In comparison, untreated cells, cells treated with 0.5 mM sodium arsenite (As) for 1 hr, or cells treated with 200 mM NaCl for 4 hr were shown. Cyan box: TDP43-mNG channel; magenta box: JF646-Halo-SEC16A channel. In "Zoom Out", arrowheads indicate coaggs, yellow boxes indicate regions shown in zoom-in views, and green dashes demarcate the nuclei. Scale bars except in "Zoom Out" represent 1 μm, and represent 5 μm in "Zoom Out". **b** Quantification of the experiments as in (**a**) and Fig. 2b showing the volume percentage (% [v/v]) of SEC16A inclusions that enrich TDP43 under the indicated conditions. $n = 45$ cells examined over 3 independent experiments. The values of individual cells are plotted as dots, and the mean values of cells in the same experiment as horizontal segments, the median of which is elongated and thickened. Different colors denote different experiments. Asterisks and "ns" respectively stand for significant (unadjusted p-value ≤ 0.05) and non-significant (unadjusted p-value > 0.05) in two-sided t-tests between the experimental means of untreated and each other condition. **c** Selected frames from a timelapse recording of ERES in a cell shifted to 42 °C. Imaging started at 60 min after the temperature shift. Cyan: TDP43-mNG; Magenta: JF646-Halo-SEC16A. The scale bar represents 1 μm. A representative timelapse of 3 independent experiments is shown. **d** Quantification of the experiment in (c) showing the relative intensities of SEC16A and TDP43 over time in ERES (normalized to their respective initial values). **e** Representative images of SEC24C or SEC31A immunostaining in cells with TDP43/SEC16A coaggs. Arrowheads: coaggs; triangles: SEC16A inclusions without TDP43. The scale bar represents 1 μm. **f**, **g** Quantification of the experiments as in (**e**) showing the percentage of TDP43/SEC16A coaggs that contained SEC24C (f) or SEC31A (g), compared with that of SEC16A inclusions without TDP43 in the same cells or in cells without TDP43/SEC16A coaggs. $n = 60$ cells examined over 3 independent experiments. The values of individual cells are plotted as dots, and the mean values of cells in the same experiment as horizontal segments, the median of which is elongated and thickened. Different colors denote different experiments. Asterisks stand for significant (p-value ≤ 0.05) in two-sided t-tests. **h** Quantification of the experiments as in (**e**) showing that the volume percentage of mature ERES (defined as SEC16A/SEC31A inclusions) that contained TDP43 in cells with TDP43-ERES. $n = 60$ cells examined over 3 independent experiments. The values of individual cells are plotted as dots, and the mean values of cells in the same experiment as horizontal segments, the median of which is elongated and thickened. Different colors denote different experiments. **i** Representative images of the ER-localization of TDP43/SEC16A coaggs (indicated by arrowheads) and SEC16A inclusions without TDP43 (indicated by triangles). The scale bar represents 1 μm. The timelapse recording can be found in Supplementary Movie 3. **j** Quantification of the experiments as in (**i**) and Supplementary Movie 3 showing the percentage of frames in which all TDP43/SEC16A coaggs or all SEC16A inclusions without TDP43 were associated with the ER. As a control, the percentage of ER-residing frames of simulated, randomly distributed particles of the same number and sizes as TDP43/SEC16A coaggs is shown. $n = 45$ cells examined over 3 independent experiments. The values of individual cells are plotted as dots, and the mean values of cells in the same experiment as horizontal segments, the median of which is elongated and thickened. Different colors denote different experiments. The asterisk and "ns" respectively stand for significant (p-value ≤ 0.05) and non-significant (p-value > 0.05) in two-sided t-tests.

## TDP43-ERES are non-dynamic (solid-like) aggregates distinct from SGs or ordinary ERES

In contrast to their highly dynamic nature in SGs or ERES without TDP43[15,54], molecules of both TDP43 and SEC16A are immobile in TDP43-ERES. In fluorescence recovery after photobleaching (FRAP) experiments, FP-tagged TDP43 and SEC16A in TDP43-ERES were partially photobleached, but the bleached and unbleached regions hardly mixed over time (Fig. 4a, b, Supplementary Movie 5). Quantification of the FRAP data yielded the mobile fractions of TDP43 and SEC16A molecules in coaggs to be roughly 15% and 10%, respectively (Fig. 4c). By contrast, TDP43 and G3BP1 in SGs rapidly and fully mixed after partial photobleaching (Supplementary Fig. 7a, b, Supplementary Movie 6) with mobile fractions of each protein to be above 60% (Fig. 4c).

The non-dynamic (solid-like) nature of TDP43-ERES was also reflected by a lack of exchange with the cytosol: when co-aggregated TDP43 and SEC16A were photobleached entirely, the fluorescence recovery for either protein was below 20% over 2.5 min (Fig. 4d–f, Supplementary Movie 7). On the other hand, TDP43 and G3BP1 in SGs rapidly exchanged with the cytosol (Supplementary Fig. 7c–e, Supplementary Movie 8) with more than 55% exchangeable with the cytosol (Fig. 4f).

Lastly, TDP43-ERES were resistant to 1,6-hexanediol (Hex) (Fig. 4g, h), which disrupts weakly aggregated macromolecules[77]. In fact, Hex treatment led to a ~30% increase in the number of TDP43-ERES due to the formation of new TDP43/SEC16A coaggs in some cells (Fig. 4h, Supplementary Movie 9). By contrast, after Hex treatment for 15 min, ~50% of SEC16A inclusions without TDP43 regardless of size and nearly all SGs dissolved (Fig. 4g, h, Supplementary Fig. 7f–h), consistent with previous reports[65,66,78]. Together, the above findings demonstrated that TDP43-ERES were non-dynamic (solid-like) aggregates distinct from SGs and ordinary ERES.

## TDP43 aggregation with ERES impairs ER-to-Golgi transport

As ERES is critical for vesicular transport from ER to Golgi, we examined whether TDP43-ERES aggregation compromises its function. Retention Using Selective Hooks (RUSH) is a method in which secretory substrates, such as ManII or TNFα, fused with streptavidin-binding protein (SBP), can be artificially retained in the ER by interaction with the streptavidin anchor. Addition of biotin then releases the retained substrates to enable quantitative analysis of protein trafficking (Supplementary Fig. 8a)[79]. We introduced the RUSH system into cells expressing TDP43-mNG and Halo-SEC16A and assayed ER-to-Golgi transport of ManII-SBP-mCherry (RUSH-ManII) under heat stress. As expected, in the absence of biotin, RUSH-ManII was retained in the ER and not delivered to Golgi, regardless of whether TDP43 aggregated in ERES (Supplementary Fig. 8b). After incubation with biotin for 1 hr, RUSH-ManII appeared in Golgi in most cells without TDP43-ERES and was no longer seen in the ER (Fig. 5a, b, Supplementary Fig. 7c). By contrast, in cells with extensive TDP43-ERES aggregation (> 10% SEC16A inclusions with TDP43), a considerable fraction of RUSH-ManII remained in the ER and outside Golgi (Fig. 5a, b). Furthermore, overexpression of TDP43-mNG but not mNG alone significantly increased the fraction of cells that displayed ER export defect (Fig. 5c), supporting that accumulated TDP43 impaired ER-to-Golgi transport.

Notably, RUSH-ManII was retained in TDP43-ERES after biotin addition for 1 hr (Fig. 5d), suggesting that TDP43 aggregation caused ERES dysfunction to trap secretory cargos recruited to these abnormal sites. To directly test this hypothesis, we took advantage of another RUSH reporter, TNFα-SBP-mCherry (RUSH-TNFα), which is pre-enriched in ERES prior to biotin supplement[56]. After adding biotin, ordinary ERES that already accumulated RUSH-TNFα efficiently exported this substrate via characteristic tubular transport intermediates/vessels (Fig. 5e), consistent with previous observations[56]. As such, the intensity of RUSH-TNFα in ordinary ERES decreased dramatically after cargo release while SEC16A intensity remained relatively stable (Fig. 5f, Supplementary Movie 10). By contrast, TDP43-ERES, although similarly recruited RUSH-TNFα (Supplementary Fig. 9a, b), failed to form tubular transport intermediates to release this cargo, such that the intensity of RUSH-TNFα remained stable and/or correlated with SEC16A intensity over time - the cross-correlation (CC) between RUSH-TNFα and SEC16A intensities was close to 1 (Fig. 5g, h, Supplementary Movie 11). We hence calculated the CC between RUSH-TNFα and SEC16A intensities for TDP43-ERES and ordinary ERES in our timelapse recordings and defined CC ≥ 0.5 as the benchmark for cargo retention. Based on this criterion, the percentage of TDP43-ERES that retained RUSH-TNFα was significantly higher than that of ordinary ERES (Fig. 5i). Surprisingly, in cells with TDP43-ERES, a lower

https://doi.org/10.1038/s41467-024-52706-7

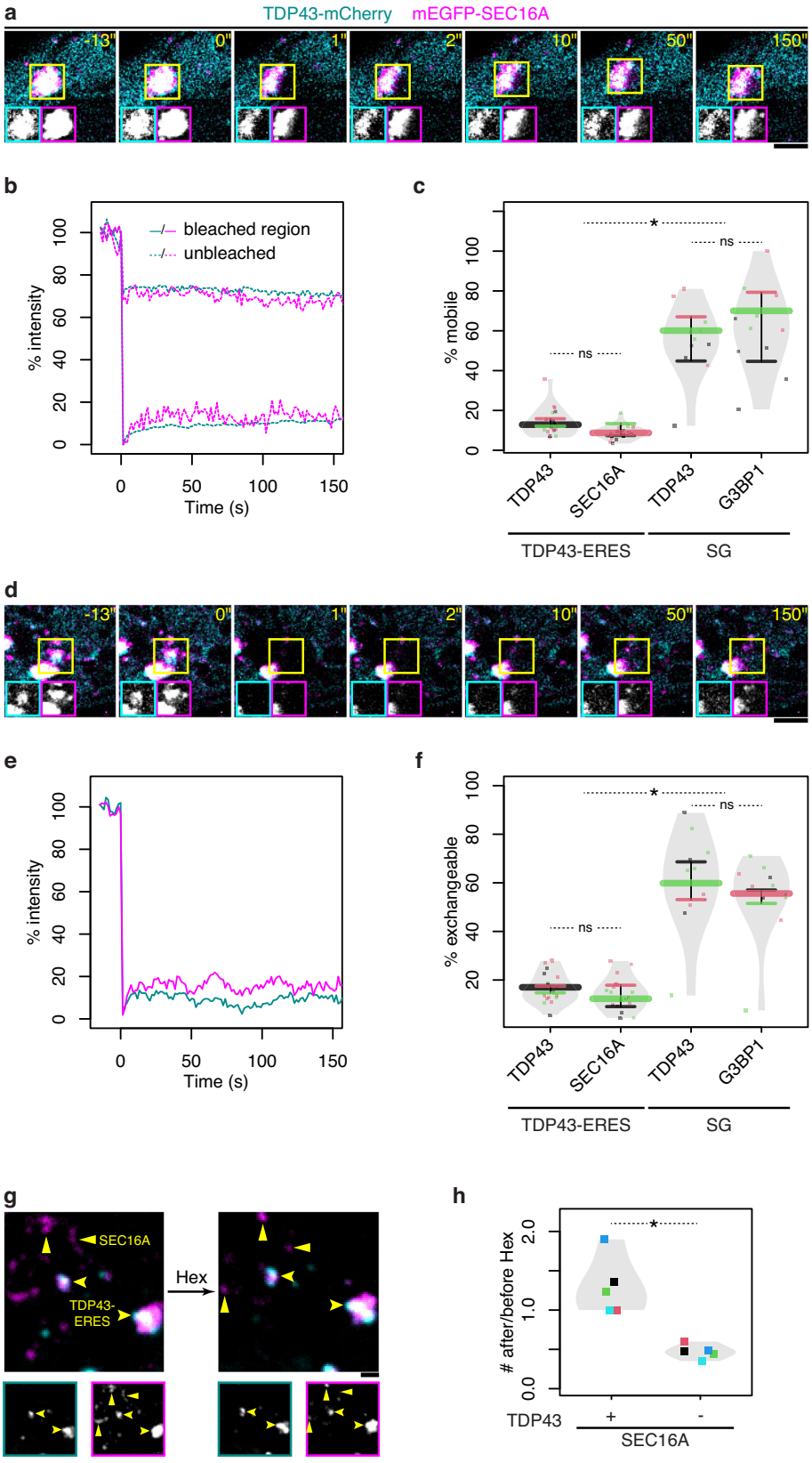


percentage of SEC16A inclusions without TDP43 enriched RUSH-TNFα (Supplementary Fig. 9a, b) and were more likely to fail in cargo release (Supplementary Fig. 9d, e, Fig. 5i, Supplementary Movie 12), suggesting that TDP43-ERES had dominant effects over ordinary ERES in the same cells.

### Artificially induced TDP43 aggregation at ERES inhibits ER-to-Golgi transport

To further investigate whether TDP43-ERES aggregation (but not cytosolic TDP43, overexpressed SEC16A, or any pleiotropic effects of the heat stress) was the cause of ERES dysfunction, we employed a

**Fig. 4 | TDP43-ERES are non-dynamic (solid-like) aggregates. a** Selected frames from a representative timelapse recording of a TDP43-ERES coagg after partial photobleaching. Insets show individual channels of the yellow boxed region. Each scale bar represents 1 µm. **b** Quantification of the experiment in (A) showing the relative intensities of TDP43 (cyan lines) and SEC16A (magenta lines) in bleached (solid lines) and unbleached regions (dashed lines) over time. **c** Quantification of partial-FRAP experiments as in (a) and Supplementary Fig. 7a comparing the mobile fractions of proteins in TDP43-ERES versus SGs. $n = 15$ aggregates examined over 3 independent experiments. The values of individual aggregates are plotted as dots, and the mean values of aggregates in the same experiment as horizontal segments, the median of which is elongated and thickened. Different colors denote different experiments. Asterisks and "ns" respectively stand for significant (p-value ≤ 0.05) and non-significant (p-value > 0.05) in two-sided t-tests. **d** Selected frames from a representative timelapse recording of a TDP43-ERES after photobleaching in its entirety. The yellow box marks the position of the coagg immediately before photobleaching. The scale bar represents 1 µm. **e** Quantification of the experiment in (**d**) showing the relative intensities of TDP43 (cyan line) and SEC16A (magenta line) over time. **f** Quantification of full-FRAP experiments as in (**d**) and Supplementary Fig. 7c comparing the exchangeable fraction of proteins in TDP43-ERES versus SGs. $n = 15$ aggregates examined over 3 independent experiments. The values of individual aggregates are plotted as dots, and the mean values of aggregates in the same experiment as horizontal segments, the median of which is elongated and thickened. Different colors denote different experiments. Asterisks and "ns" respectively stand for significant (p-value ≤ 0.05) and non-significant (p-value > 0.05) in two-sided t-tests. **g** Representative images showing TDP43-ERES (indicated by arrowheads) and SEC16A inclusions without TDP43 (indicated by triangles) in a cell before and after 3.5% [v/v] 1,6-hexanediol (Hex) treatment for 15 min. Insets show individual TDP43-mCherry (cyan) and mEGFP-SEC16A (magenta) channels. The scale bar represents 1 µm. **h** Quantification of the experiments as in (**g**) comparing the after/before ratios of TDP43-ERES and SEC16A inclusions without TDP43. $n = 50$ cells examined over 5 independent experiments. The median values of cells in the same experiments are plotted as dots. The asterisk stands for significant (p-value ≤ 0.05) in two-sided t-test.

method to directly aggregate TDP43 in ERES. When TDP43 and SEC16A were respectively fused with three copies of FKBP and FKBP-rapamycin binding domain bearing T2098L mutation (FRB*), the rapamycin analog AP21967 (AP), which dimerizes FKBP and FRB*, directly induced TDP43/SEC16A co-aggregation (Supplementary Fig. 9f). As a control, cells expressing TDP43 and SEC16A without FKBP or FRB* tagging were not responsive to AP (Supplementary Fig. 9g, Fig. 6a, b). Furthermore, like the TDP43-ERES induced by proteotoxic stresses, AP-induced TDP43/SEC16A coaggs contained COPII proteins (Fig. 6c), and 3xFKBP-TDP43-mNG and 3xFRB*-Halo-SEC16A molecules inside were immobile as revealed by FRAP (Fig. 6d).

Next, we examined whether AP-induced TDP43 aggregation at ERES affected cargo export from the ER. The AP-induced TDP43-ERES still enriched RUSH-TNFα (Fig. 6a), but this cargo was not exported after biotin addition (Fig. 6e, f, Supplementary Movie 13). By contrast, in the absence of AP, cargo release from ERES was unaffected, suggesting that FKBP or FRB tagging alone did not compromise ERES function (Supplementary Fig. 9h, i, Fig. 6g). As an additional control, AP-induced recruitment of 3xFKBP-mNG to ERES but did not cause ERES to retain RUSH-TNFα (Supplementary Fig. 9j, k, Fig. 6g). These results suggest that TDP43 aggregation in ERES is sufficient to impair ER-to-Golgi transport (Fig. 6h).

### TDP43-ERES are found in motor neurons of ALS patients

It was recently proposed that the diffuse punctate cytoplasmic staining (DPCS) of TDP43 are aggregates on the ER membrane and an early-stage pathology of ALS[24]. In addition, motor neurons derived from the human induced pluripotent stem cells (hiPSCs) of ALS patient or found in their post-mortem sections exhibit attenuated vesicle transport and activation of Unfolded Protein Response (UPR), which contribute to neuronal dysfunction and death[80–85]. We therefore tested if TDP43 aggregation in ERES is elevated in ALS patient-derived motor neurons. *C9ORF72* is the most mutated gene in ALS patients[86,87]. We induced motor neurons (iMNs) from human embryonic stem cells (hESCs) or hiPSCs derived from ALS patients bearing *c9orf72* (*c9*) mutations (NDS00268, NDS00269 and NDS00270) and non-ALS (control) individuals (BJ, GM23720 and H9) (Supplementary Fig. 10a, b), and stained TDP43 and SEC16A by immunofluorescence. ALS patient-derived iMNs displayed significantly increased level (volume percentage) of TDP43-ERES (Fig. 7a, b).

About 90% of ALS cases are characterized as sporadic ALS (sALS)[88], so we used immunofluorescence staining to analyze TDP43/SEC16A co-aggregation in the post-mortem brain sections of 10 sALS and 1 familial ALS (fALS) patients. In neurons of the (ALS-affected) motor cortex but not the (unaffected) occipital cortex, TDP43 linear wisps (fibril-like aggregates) could be observed in the cytoplasm while TDP43 were depleted from the nucleus (Supplementary Fig. 10c, d), as previously reported[10,89]. In the motor cortex, TDP43-ERES were found at significantly higher level compared with the occipital cortex (Fig. 7c, d, Supplementary Fig. 10e). Paired motor-occipital cortices analysis was performed for each patient to calculate the fold change (FC) of TDP43/SEC16A coaggs in motor cortex as compared with occipital cortex (Supplementary Fig. 10f). The FCs of 5 patients fell in the range of 3-4, 2 patients showed FCs above 10, and the remaining 4 was largely unchanged (Supplementary Fig. 10f). Notably, the morphology and subcellular distribution of TDP43-ERES were similar to those of DCPS, i.e. both are diffusive puncta in the cytoplasm (Fig. 7c). In addition, we observed skein-like TDP43 aggregates in the extracellular space of the motor cortex but not occipital cortex (Fig. 7e, f), and most of these TDP43 skeins contained SEC16A (Fig. 7e, g). Notably, along these TDP43/SEC16A skeins, there were high intensity cores of SEC16A (Fig. 7h, Supplementary Fig. 10g), which resembled the clustered form of TDP43-ERES observed in heat stressed RPE-1 cells (Fig. 3c, Supplementary Fig. 5d). In 1 out of 11 patients examined, intracellular skein-like TDP43/SEC16A aggregates were observed along with extracellular skeins (Fig. 7i, Supplementary Fig. 10h). Thus, TDP43 aggregation at ERES is associated with ALS cellular pathology, but the causal relationship requires further investigation.

## Discussion

Protein aggregation, or clumping, results in the formation of dynamic (liquid-like) or non-dynamic (solid-like) inclusions. Recently, it was found that SGs and nucleoli can undergo phase transition from dynamic to non-dynamic aggregates by accumulating misfolded proteins[16,17,53]. In the present study, we utilized Hsp104$^{DWB}$-mEGFP-FLAG in an affinity-based approach to identify the protein components of aggregates that contain misfolded proteins in human HEK293T cells, which was selected as a basic cell biology model to identify proteins of high aggregation propensity under stress, although future work is needed to validate the identified aggregating proteins of particular relevance to ALS in more appropriate cell types and samples. Among the 337 aggregation-prone proteins identified, there are not only components of SGs and nucleoli but also SEC16A, which was suggested to undergo LLPS to constitute the scaffold of ERES[54,55,57]. Our data further show that, under heat stress, a fraction of ERES contain misfolded proteins as revealed by Hsp104$^{DWB}$-mEGFP binding, and some accumulate TDP43 and become non-dynamic (solid-like). Therefore, ERES are a new type of precursors for non-dynamic aggregate formation. Whereas TDP43-containing SGs can remain dynamic (liquid-like) for hours to days[15–17], ERES turn non-dynamic soon after stress- or AP-induced TDP43 aggregation. Importantly, SGs that remain in dynamic (liquid-like) state have been proposed to play certain cytoprotective roles, such as storing mRNAs

https://doi.org/10.1038/s41467-024-52706-7

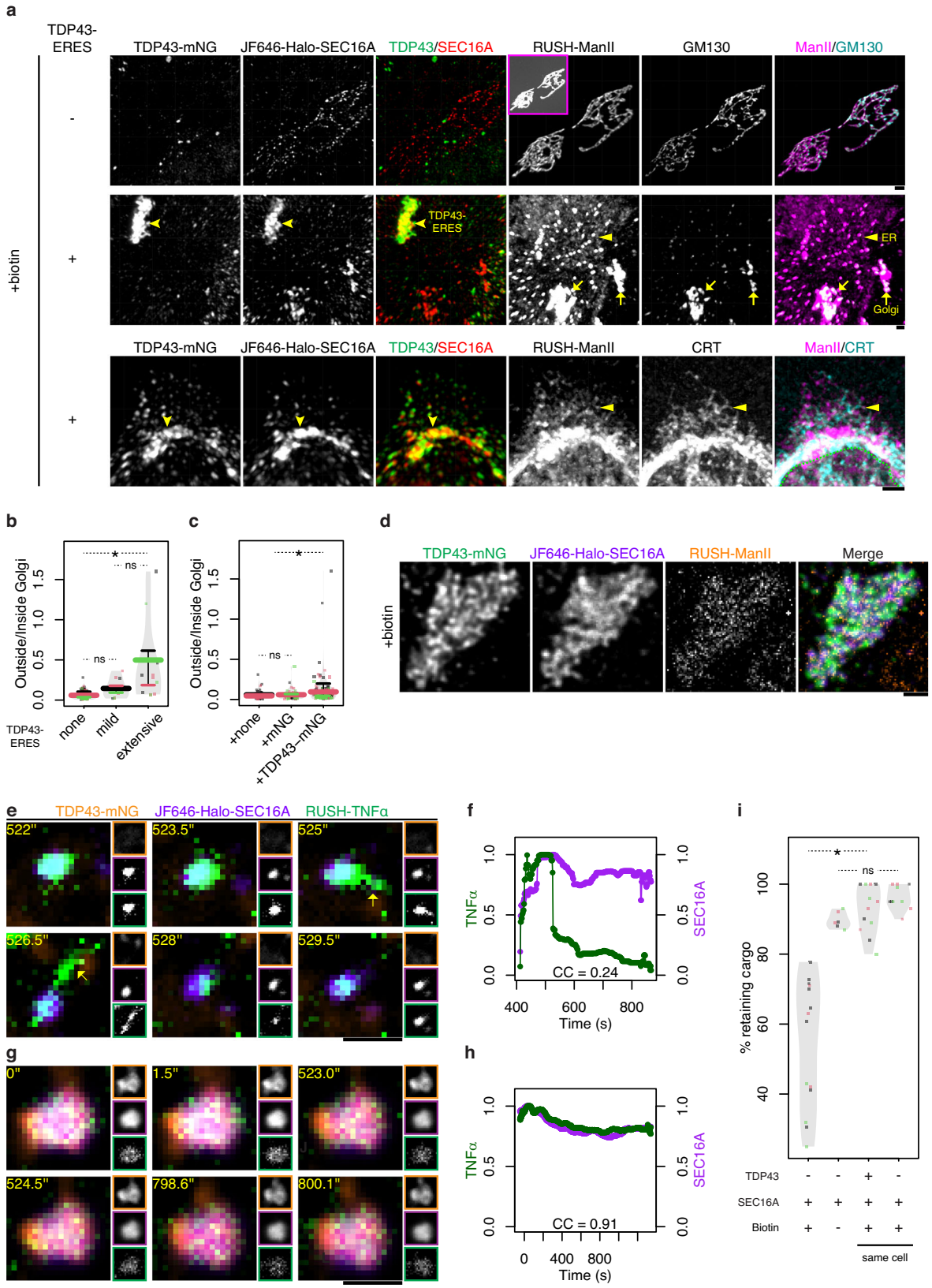


other than those involved in stress response[90–92], although SGs can also be crucibles for non-dynamic (solid-like) aggregate formation during prolonged stress[16,17]. In this study, we observed that SG formation suppresses TDP43 aggregation at ERES, which might represent another aspect of cytoprotection by SGs worthy of further exploration. Moreover, RNA-binding and post-translational modifications, such as phosphorylation and ubiquitination, may also influence TDP43 aggregation with SG or ERES.

Previous studies showed that 40-60% of TDP43 is synthesized by ER-attached ribosomes by ribosome profiling[93,94], and TDP43 can interact with lipid bilayers through its prion-like domain[95], which may contribute to its concentration on the ER surface and recruitment to

**Fig. 5 | TDP43-ERES aggregation impairs ER-to-Golgi transport. a** Representative images of RUSH assays in cells without or with TDP43 co-aggregation with ERES. After biotin addition for 1 hr, the subcellular localization of ManII-SBP-mCherry (RUSH-ManII) was imaged with GM130 (Golgi marker) or calreticulin (CRT – ER marker) visualized by using immunofluorescence staining. The inset shows a contrast-adjusted view; arrowheads indicate TDP43-ERES; arrows point to fragmented Golgi; triangles point to RUSH-ManII retention in the ER; green dashes demarcate the nucleus. The 3D projections (view from top) of these cells are displayed. Each scale bar represents 1 µm. **b** Quantification of the experiments as in (**a**) and Supplementary Fig. 8c showing the ratios between RUSH-ManII intensity outside and inside Golgi. Cells were categorized based on their volume percentage of TDP43-ERES (none: 0%; mild: 0-10%; severe: ≥ 10%). $n = 45$ cells examined over 3 independent experiments. The values of individual cells are plotted as dots, and the mean values of cells in the same experiment as horizontal segments, the median of which is elongated and thickened. Different colors denote different experiments. The asterisk and "ns" respectively stand for significant (p-value ≤ 0.05) and non-significant (p-value > 0.05) in two-sided t-tests. **c** Quantification of cells transfected with RUSH-ManII and Halo-SEC16A only or additionally with mNG or TDP43-mNG showing the outside/inside Golgi ratios of RUSH-ManII intensity. n = 45 cells examined over 3 independent experiments. The values of individual cells are plotted as dots, and the mean values of cells in the same experiment as horizontal segments, the median of which is elongated and thickened. Different colors denote different experiments. The asterisk and "ns" respectively stand for significant (p-value ≤ 0.05) and non-significant (p-value > 0.05) in two-sided t-tests. **d** Representative images of TDP43-ERES trapping RUSH-ManII after biotin addition for 1 hr. A representative slice of the z-stack is displayed. The scale bar represents 1 µm. **e** Selected frames of a representative timelapse recording of an ordinary ERES (in a cell without TDP43-ERES) during RUSH-TNFα transport from ER to Golgi. Biotin was added at 0". Arrows indicate the budding of a tubular transport intermediate. The scale bar represents 1 µm. **f** Quantification of relative RUSH-TNFα intensity over time (normalized to the max intensity), compared to the relative intensity of SEC16A in the ERES tracked in (e). CC: cross-correlation between RUSH-TNFα intensity and SEC16A intensity. **g** Selected frames of a representative timelapse recording of a TDP43-ERES during RUSH-TNFα assay. The scale bar represents 1 µm. **h** Quantification of RUSH-TNFα and SEC16A intensities over time (normalized to their respective max intensities) in the TDP43-ERES tracked in (**g**). **i** Quantification of the percentage of TDP43-ERES and ERES without TDP43 in either the same or different cells that retained RUSH-TNFα in the experiments as in (**e**–**h**) and Supplementary Fig. 9d, e. The criterion for cargo retention is CC ≥ 0.5. $n = 9$ cells examined over 3 independent experiments. Cells without biotin supplement were included as a control. $n = 6$ cells examined over 3 independent experiments. Each dot represents one cell, and different colors denote different experiments. The asterisk and "ns" respectively stand for significant (p-value ≤ 0.05) and non-significant (p-value > 0.05) in two-sided t-tests.

ERES. In addition, ERES was recently shown to form at highly connected regions of the ER with "high search rate" and consist of interwoven networks of membranes[56,96], which potentially traps the newly synthesized TDP43. Speculatively, when enriched at ERES, the prion-like C-terminal domain of TDP43 could interact directly with the intrinsically disordered region (IDR) of SEC16A, which spans more than 50% of the latter's sequence[57,97]. Consistent with our previous findings in yeast that stress-induced aggregates emerge from the cytoplasmic surface of the ER and are likely to be seeded by newly synthesized proteins[33], in this study, we found that the nascent TDP43 is more prone to aggregation in ERES than pre-existing TDP43 and blocking protein synthesis by CHX strongly suppressed such aggregation. This may be explained by a combination of the proximity of nascent TDP43 to ERES, the fact that newly synthesized proteins are more prone to stress-induced misfolding and damage[98,99], and possibly a lack of RNA-binding or certain post-translational modifications on nascent TDP43[15]. The preferential aggregation of nascent TDP43 with ERES may also help explain the observation that acute arsenite treatment did not induce TDP43/SEC16A coaggs or high-level cytoplasmic or SG accumulation of TDP43. It is possible that the cytoplasmic accumulation under the more prolonged proteotoxic stress was due to impaired nuclear transport of TDP43 newly synthesized in the cytoplasm. Indeed, several NPC proteins, such as NUP214 and NUP88, were enriched in aggregates. These nucleoporins could be incorporated into cytoplasmic aggregates either as newly synthesized or damaged proteins or perhaps during mitosis, when NPCs undergo disassembly after nuclear envelope breakdown[100]. Such stress-induced cytoplasmic foci of nucleoporins have also been reported in *C. elegans*[101].

TDP43-ERES are usually larger in size than ordinary ERES, like the recently reported Sec bodies (SBs), which are enlarged ERES (> 300 nm in radius) retaining dynamic (liquid-like) properties[65,66]. However, TDP43-enriched ERES are distinct from SBs in multiple aspects. First, pronounced SBs were found only in *Drosophila melanogaster* (fruit fly) S2 cells and a specific mammalian cell line, the rat insulinoma INS-1, but not in several other cell lines studied[66]. By contrast, we observed TDP43-enriched ERES in multiple human cell lines of different tissue origins, including RPE-1, HEK293T and motor neurons. Second, SBs were induced under specific conditions such as high NaCl concentration[66] whereas TDP43-enriched ERES were induced by various proteotoxic stresses but not NaCl supplement. Lastly, SBs are dynamic (liquid-like) structures whereas ERES that assimilated TDP43 were non-dynamic (solid-like). However, the above differences cannot rule out a possible link between SBs and TDP43.

It has been questioned whether protein aggregation is the cause or result of cellular dysfunction and whether aggregation is protective against proteotoxic damages[21,102–107]. Our findings suggest that TDP43 aggregation in ERES is deleterious, as it compromises the function of ERES in cargo export from the ER. Our data also suggest that TDP43-ERES exerts a dominant effect over ordinary ERES, potentially through sequestration of COPII subunits or other limiting factors regulating COPII vesicle release. As such, when TDP43 aggregates in over 10% of SEC16A inclusions, the ER-to-Golgi transport is globally delayed. As TDP43-ERES are non-dynamic aggregates with limited exchange of molecules with the cytosol, they cannot spontaneously disassemble. Therefore, the inhibitory effect of TDP43-ERES aggregation on the secretory pathway may not be readily reversed after stress attenuation, which would be different from the regulatory inhibition of ER export by reversible SG recruitment of SEC23 and SEC24, but not SEC16A, reported previously[108].

We observed that TDP43-ERES could recruit cargos but not generate tubular transport vessels to release them, suggesting that TDP43-ERES are defective in COPII vesicle budding. Such dysfunction could result from the inhibitory effect of TDP43 on the GTPase cycle of COPII complex, or on the mechanics of vesicle budding due to liquid-to-solid phase transition associated with TDP43 aggregation. Recent studies suggest that dynamic (liquid-like) assemblies can promote membrane bending or budding under certain conditions[109,110]. Such potential effect of SEC16A condensates on the ER membrane could be disrupted by TDP43-induced phase transition. Moreover, ERES was recently found to generate tubule vessels of connected COPII vesicles rather than separate ones as the transport intermediate[56], and solid-like aggregates might mechanically block the elongation of these pearled tubules. It was recently found that the efficiency of ERES to export cargos directly positively correlates with the dynamic properties of the SEC16A scaffold, which is tightly regulated by the kinase DYRK3 and an unknown phosphatase[57]. In addition, the COPII protein SEC24 also form highly dynamic (liquid-like) aggregates at ERES, but its dynamic property is reduced by increasing concentrations of manganese ions ($Mn^{2+}$) while the size of mature ERES increases, so the export rate of lipoprotein cargos increases with $Mn^{2+}$ concentrations at low $Mn^{2+}$ doses but decreases again at higher doses. Such $Mn^{2+}$-based regulation can be hijacked by adenovirus to influence lipid homeostasis[111]. Our

https://doi.org/10.1038/s41467-024-52706-7

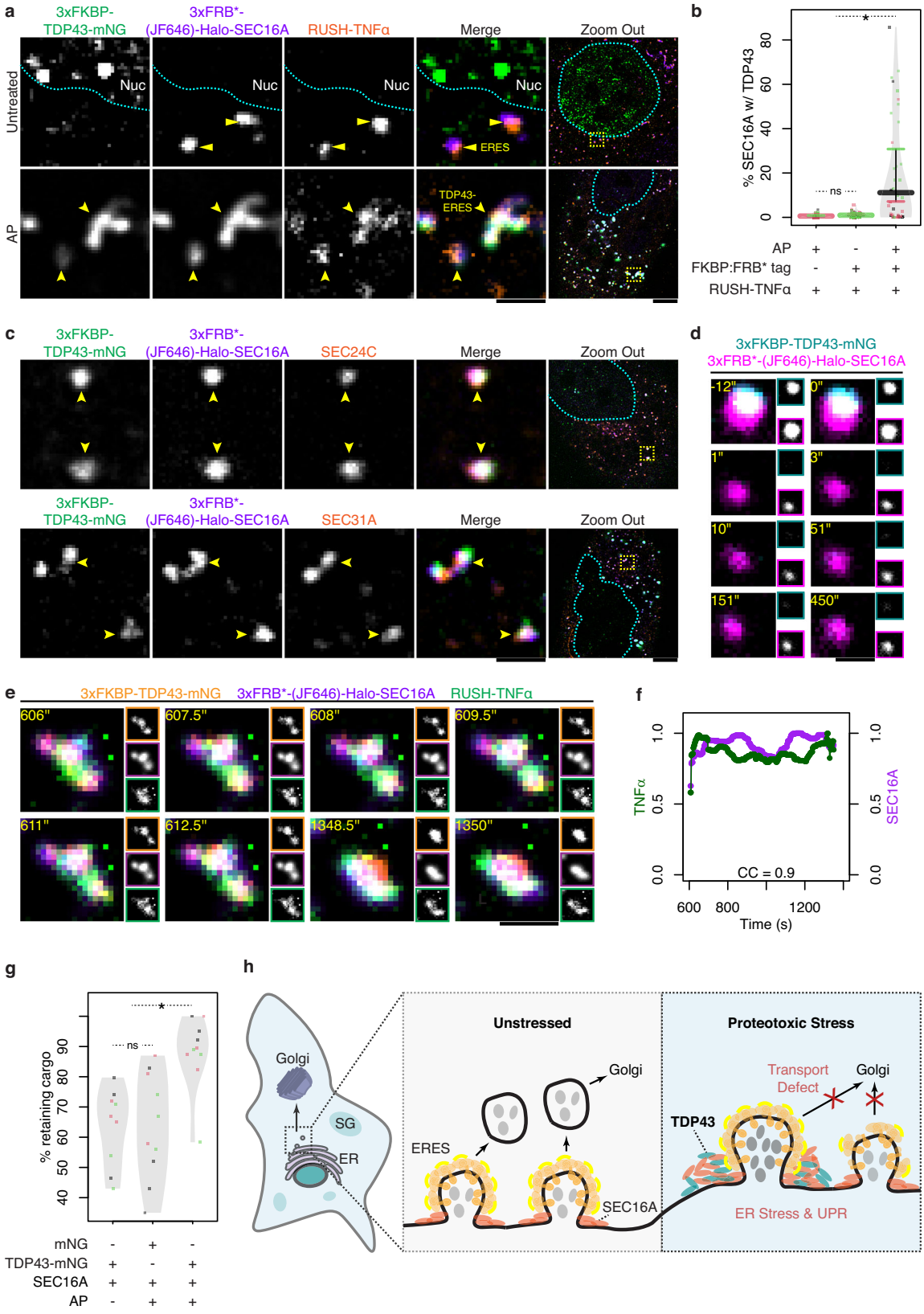


study adds another pathogenic mechanism that decreases ERES functionality.

On average, ~15% of mature ERES co-aggregated with TDP43 in RPE-1 cells under the stress condition applied, given that <60% SEC16A-positive foci were observed to be mature ERES that had incorporated SEC24 and SEC31 and poised for COPII vesicle budding. In a small fraction of cells, 80-100% mature ERES co-aggregated with TDP43. Although TDP43 overexpression has been reported to induce aggregation and abnormal RNA splicing[112–116], the heterogeneity observed in our study was only partially explained by different overexpression

**Fig. 6 | Artificially induced TDP43-ERES retain secretory cargo. a** Representative images of cells cultured in biotin-free media expressing 3xFKBP-TDP43-mNG, 3xFRB*-Halo-SEC16A and RUSH-TNFα without or with AP21967 (AP) treatment for 6-10 hr. Arrowheads and triangles indicate TDP43-ERES and ordinary ERES, respectively. In "Zoom out", yellow boxes mark the regions displayed in zoom-in views, and cyan dashes demarcate the nuclei. Scale bars except in "Zoom Out" represent 1 µm, and represent 5 µm in "Zoom Out". **b** Quantification of the experiments as in (**a**) and Supplementary Fig. 9 g showing the volume percentage of SEC16A inclusions that enriched TDP43 under the indicated conditions. n = 45 cells examined over 3 independent experiments. The values of individual cells are plotted as dots, and the mean values of cells in the same experiment as horizontal segments, the median of which is elongated and thickened. Different colors denote different experiments. The asterisk and "ns" respectively stand for significant (p-value ≤ 0.05) and non-significant (p-value > 0.05) in two-sided t-tests. **c** SEC24C or SEC31A immunostaining in cells with AP-induced TDP43/SEC16A coaggs. Scale bars except in "Zoom Out" represent 1 µm, and represent 5 µm in "Zoom Out". Representative images of 3 independent experiments are shown. **d** Selected frames from a timelapse recording of an AP-induced TDP43-ERES after photobleaching. Insets show individual channels. 3xFKBP-TDP43-mNG was entirely photobleached whereas 3xFRB*-(JF646)-Halo-SEC16A was partially bleached. The scale bar represents 0.5 µm. A representative timelapse of 3 independent experiments are shown. **e** Selected frames of a representative timelapse recording of an AP-induced TDP43-ERES during RUSH-TNFα assay. The scale bar represents 1 µm. **f** Quantification of RUSH-TNFα and SEC16A intensities over time (normalized to their respective max intensities) in the TDP43-ERES tracked in (**e**). **g** Quantification of the percentage of AP-induced TDP43(-mNG)-ERES, mNG-ERES and ERES without TDP43 (in cells without AP treatment) that retained RUSH-TNFα in the experiments as in (**e**) and Supplementary Fig. 9h–k. $n = 9$ cells examined over 3 independent experiments. Each dot represents one cell, and different colors denote different experiments. The asterisk and "ns" respectively stand for significant (p-value ≤ 0.05) and non-significant (p-value > 0.05) in two-sided t-tests. **h** Working model of TDP43 aggregation at ERES causing retention of transport cargos. TDP43-ERES also exert a dominant effect over ordinary ERES in the same cells possibly through sequestration of essential transport factors. The ER-to-Golgi transport defect caused by TDP43-ERES co-aggregation may further induce ER stress.

levels of TDP43 and SEC16A, as shown by Pearson's correlation analyses. The heterogeneity was also observed in immunostained iMNs and MNs in the postmortem samples, which is consistent with previous studies on protein aggregation[10,112–115]. It has also been suggested that the underlying cause for the heterogeneous protein aggregation is the heterogeneity in stress tolerance among cells, such as SG formation in the case of TDP43/SEC16A, or stochasticity in the nucleation of protein aggregation[116,117].

In some iMNs and MNs in postmortem samples, the percentage of SEC16A foci that colocalize with TDP43 aggregates was above 10%. Based on our findings in RPE-1 cells, it is reasonable to speculate that the percentage of mature ERES with TDP43 aggregation could be much higher. Importantly, the partial co-aggregation and inhibition of transport is not unexpected for a cellular defect that contributes to ALS. In fact, the cellular defects underlying ALS disease onset and progression are unlikely to be homogeneous full-scale blockage of an essential cellular process, as ALS is an age-associated progressive disease[88,118,119]. Furthermore, TDP43 pathology in MNs is highly dependent on ALS disease stage or duration[24,120]. If TDP43-ERES were early ALS pathology, then its abundance in postmortem samples could decrease or diminish, and the morphology could differ substantially from the co-aggregates initially formed intracellularly. Although the origin of intracellular or extracellular TDP43/SEC16A skeins is still elusive, it is conceivable that they could result from clustered TDP43-ERES aggregates and released after cell death.

Supporting the disease relevance of our findings, SEC16A mutations were identified as a potential risk factor for ALS in one recent study that integrates functional genomics with genome-wide association study (GWAS)[121], and defects in intracellular vesicle transport were reported in ALS patient iMNs[122]. In addition, activation of UPR (conceivably caused by ER stress) leading to ER expansion is a widely recognized hallmark of ALS pathology[80–84]. Previous studies indicated that ER-to-Golgi transport is inhibited by certain TDP43, SOD1, FUS or UBQLN2 mutants[123,124], which, however, are rare among ALS patients[86,87]. Our findings on the harmful TDP43 aggregation in ERES suggest a more general mechanistic explanation for the observation of ER stress markers in postmortem samples. Given the morphological similarity between intracellular TDP43-ERES co-aggregates and the DPCS, further exploration could be conducted to evaluate whether this type of aggregates could potentially serve as an early diagnostic marker or therapeutic target for alleviating the toxic effects of TDP43 aggregation in ALS.

## Methods

This research complies with relevant ethical regulations and protocols are approved by NUS Office of Safety Health and Environment.

### Mammalian cell culture and plasmid transfection

Cell culture was performed according to the American Type Culture Collection (ATCC) guidelines with minor modifications. Briefly, RPE-1 cells were maintained in DMEM:F12 (Thermo 11320082) + 10% [v/v] FBS (Thermo 16140071) and passaged using 0.05% [w/v] trypsin solution (Thermo 25300120). HEK293T cells were cultured in DMEM (Thermo 11965118) + 10% [v/v] FBS and passaged similarly. For high-resolution microscope imaging, cells were seeded on glass-bottom dishes (Iwaki 3930-035 or 3931-035) pre-coated with 10 µg/mL fibronectin (Sigma 10838039001) overnight at 4 °C. Plasmid transfections were performed using Lipofectamine 3000 (Thermo L3000015) according to the manufacturer's protocol. The transfection amounts of different plasmids were optimized (Supplementary Data 2). Plasmids generated in this study and their maps will be submitted to Addgene and also available on request. Cells were analyzed by microscopy imaging, Western Blot (WB) or other means 24–48 hr after plasmid transfection.

### Aggregate induction and inhibitor/chemical treatments

To examine protein aggregation under different conditions, cells were either untreated, mock treated or heat stressed at 42 °C, or treated with different chemicals for 12–16 hr. MG132 (Sigma M7449), inhibitor of aspartyl proteases and cysteine proteases that are also found in proteasomes, was used at 10 µM final concentration. The autophagy inhibitor Bafilomycin A1 (Baf) (Sigma SML1661) was used at 100 nM. Sodium arsenite (Santa Cruz SC-250986) was used at 0.5 mM for 1 hr. NaCl (Axil BIO-1111) was used at 200 mM for 4 hr to replicate the condition used for Sec body (SB) induction[66]. The protein translation inhibitor cycloheximide (CHX) (Sigma C1988) was used at 20 µg/mL for 6 hr. 1,6-Hexanediol (Hex) (Sigma 88571) was used at 3.5% [v/v] and cells were imaged immediately by timelapse recording.

### HaloTag (Halo) and Immunofluorescence (IF) staining

Halo staining was performed according to the dye manufacturer's protocol with minor modifications. Briefly, Janelia Fluor 549 (JF549) or JF646 ligand (Promega GA1110 or GA1120) was added to media to a final concentration of 15–50 nM and incubated for 15-30 min or indicated time. Then cells were washed once using fresh media (unless indicated otherwise), and either imaged directly or fixed using 4% [w/v] paraformaldehyde (PFA) (EMS 15710) diluted in phosphate buffered saline (PBS) (Thermo 14190250) for 20 min at room temperature (RT). For IF staining of proteins except from calreticulin (CRT), live cells were washed once using fresh media and fixed using 4% [w/v] PFA. After three PBS washes, cells were permeabilized in PBS + 0.1% [v/v] Triton X-100 (Thermo 85111) for 10 min and blocked in PBS + 0.1% [v/v] Tween 20 (Sigma P1379) (PBST) + 1%

https://doi.org/10.1038/s41467-024-52706-7

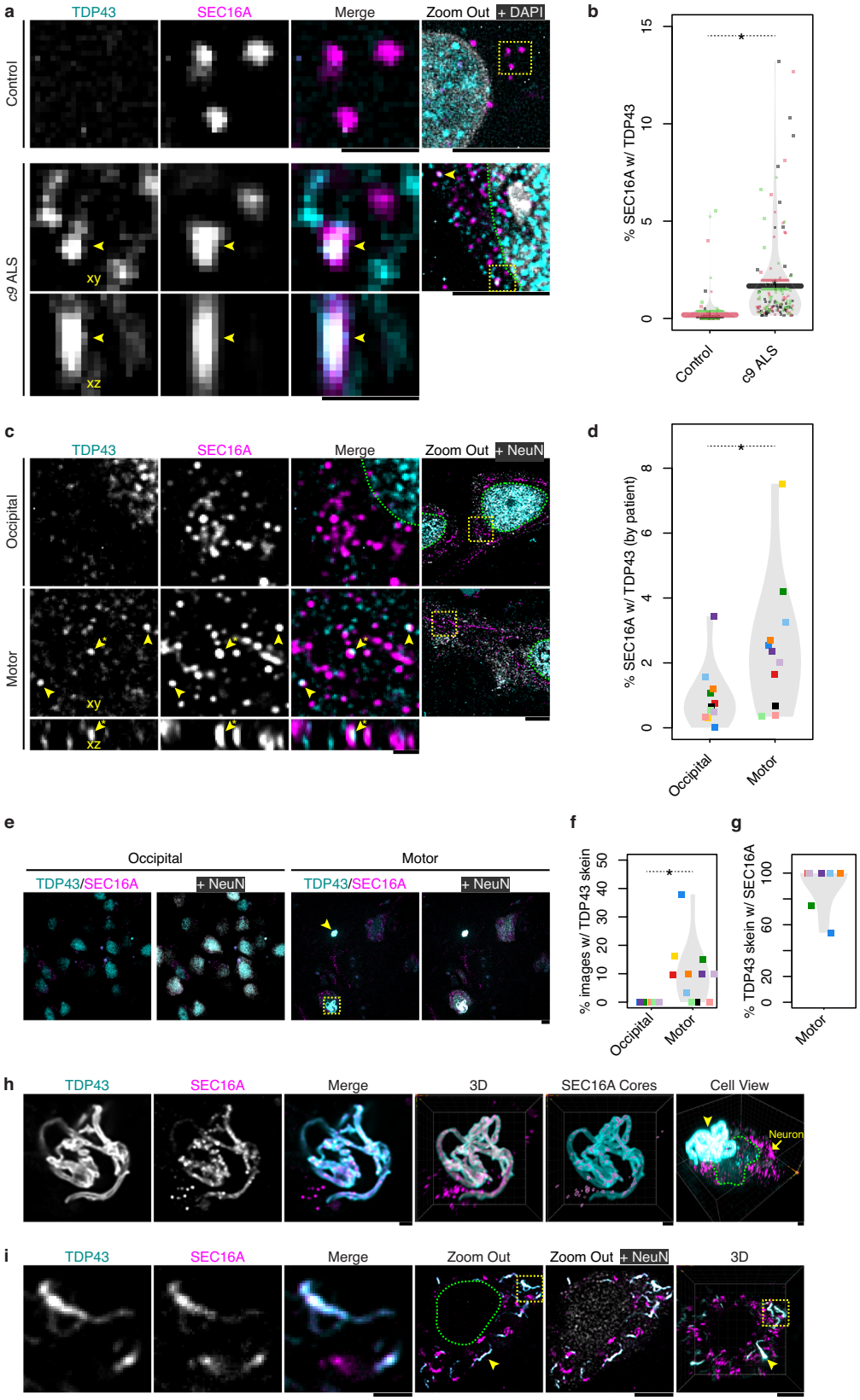


[w/v] BSA (Sigma A2153). Cells were incubated with primary antibodies overnight at 4 °C in PBST + 1% [w/v] BSA. Then after four washes with PBS, cells were incubated with fluorophore-conjugated secondary antibodies in the same diluent for 1 hr at RT. Again, cells were washed four times using PBS before microscopy imaging. For IF staining of CRT, the following modifications were made: cells were instead fixed using 2% [w/v] PFA + 1.5% [w/v] glutaraldehyde (GA, Sigma 5882) at 37 °C; after PBS washes to remove fixatives, cells were incubated for 10 min at RT with 0.1% [w/v] sodium borohydride ($NaBH_4$, Sigma 452882) in PBS to reduce GA; primary antibody incubation was reduced to 2 hr at 4 °C. Antibodies used in this study are listed in Supplementary Data 2.

**Fig. 7 | Co-aggregation of TDP43 with ERES in ALS-affected motor neurons.** **a** Representative images of immunofluorescence staining of TDP43 and SEC16A in MNs induced from a non-ALS (Control) hiPSC line (BJ) and an ALS patient hiPSC line (NDS00270) that carries the *c9orf72* mutation (*c9*). In "Zoom out", yellow boxes mark the regions displayed in zoom-in views, and green dashes demarcate the nuclei. The sectioning of the TDP43/SEC16A coagg along the **xz** plane is displayed beneath the **xy** view. Scale bars except in "Zoom Out" represent 1 µm, and represent 5 µm in "Zoom Out". **b** Quantification of the experiments as in (**a**) showing the volume percentage of SEC16A inclusions that contained TDP43. $n = 90$ cells examined in 3 normal or 3 patient hESC/hiPSC lines. The values of individual cells are plotted as dots, and the mean values of cells derived from the same hESC/hiPSC as horizontal segments, the median of which is elongated and thickened. Different colors denote different hESC/hiPSC. The asterisk stands for significant (p-value ≤ 0.05) in two-sided t-test. **c** Representative images of the immunofluorescence staining of TDP43, SEC16A and the neuronal marker NeuN (RBFOX3) in the post-mortem sections of the occipital cortex and motor cortex from the same sALS patient. The arrowheads with asterisk indicate the same TDP43/SEC16A coagg in **xy** and **xz** views. Scale bars except in "Zoom Out" represent 1 µm, and represent 5 µm in "Zoom Out". **d** Quantification of the experiments as in (**c**) showing the volume percentage of SEC16A inclusions containing TDP43 in the occipital cortex versus motor cortex of 11 different ALS patients. n = 330 z-stacks each taken from the occipital and motor cortex of 11 patients. The mean values of cells from the same patients are plotted as dots. Different colors denote different patients. The same color coding applies in (**f**), (**g**), Supplementary Fig. 10d–f. The asterisk stands for significant (p-value ≤ 0.05) in two-sided t-test. **e** Representative images of TDP43, SEC16A and NeuN immunostaining in the occipital cortex and motor cortex of the same sALS patient. 2 skein-like TDP43/SEC16A aggregates in the motor cortex are boxed and indicated by arrowhead, with their respective zoom-in views displayed in (**h**) and Supplementary Fig. 10g. The max intensity projection of confocal z-stacks is shown. The scale bar represents 5 µm. **f** Quantification of the percentage of confocal z-stack images containing skein-like TDP43 aggregates in the occipital versus motor cortex of 11 ALS patients (color-coded) in the experiments as in (**e**). $n = 330$ z-stacks each taken from the occipital and motor cortex of 11 patients. The values of individual patients are plotted as dots. The asterisk stands for significant (p-value ≤ 0.05) in two-sided t-test. **g** Quantification of the percentage of TDP43 skeins that contained SEC16A in the motor cortex of ALS patients in the experiments as in (**e**). $n = 330$ z-stacks taken from the motor cortex of 11 patients. The values of individual patients are plotted as dots. **h** Zoom-in views of the TDP43/SEC16A skein-like aggregate boxed in (**e**). "SEC16A Cores" shows the contours of high SEC16A fluorescence intensity; "Cell View" shows a neuron (indicated by the arrow) beneath the TDP43/SEC16A skein (indicated by the arrowhead), and the nucleus of this neuron is demarcated by green dashes. Each scale bar represents 1 µm. **i** Representative images showing the intracellular TDP43/SEC16A skein-like aggregates found in 2 different postmortem sections of sALS Patient 132's motor cortex. Green dashes demarcate the nucleus. Scale bars except in "Zoom Out" and "3D" represent 1 µm, and represent 5 µm in "Zoom Out" and "3D".

### RNA fluorescence in situ hybridization (FISH)

RNA FISH was performed according to a published protocol[59] with minor modifications. Briefly, cells were fixed and permeabilized as in IF, and then washed thrice in PBS and twice in SSC wash buffer (2x SSC buffer + 15% [v/v] formamide), in which the 2x SSC buffer (300 mM NaCl, 30 mM sodium citrate, pH = 7.0) was diluted from 20x SSC (Sigma S6639) using UltraPure DNase/RNase-Free Distilled Water (Thermo 10977015). Then Alexa Fluor 647 (AF647)-conjugated oligo$(dT)_{30}$ purchased form IDT was diluted to a final concentration of 1 ng/µL in FISH buffer, which consists of SSC wash buffer + 10% [w/v] dextran sulfate (Sigma D8906) + 2 mM vanadyl-ribonucleoside complex (NEB S1402) + 0.02% [w/v] BSA, + 1 mg/mL tRNA (Sigma 10109541001), and used to stain cells at 37 °C overnight. After incubation, cells were washed twice in SSC wash buffer and twice in PBS, re-fixed in 4% [w/v] PFA for 10 min at RT, and washed thrice in PBS before imaging.

### Microscopy imaging

Wide field images were taken on a EVOS M5000 microscope using a 40x air objective. Confocal images were taken on Yokogawa CSU-W1 spinning disk microscope (installed on Nikon Eclipse Ti-E inverted microscope body) with a CFI Apochromat λ 100x oil objective (NA = 1.4), Cargille Type 37 immersion oil (Cargille Labs 16237-16) and Photometrics Prime 95B Scientific CMOS cameras. Z-stacks were taken using a Piezo stage (Piano Z from Physik Instrumente) every 0.1 µm for a total thickness of 5 or 10 µm except for Supplementary Movie 9, in which the step size was 0.5 µm. To enable Structured Illumination Microscopy (SIM), the Live-SR super-resolution module (Roper Scientific) was engaged except for Figs. 4, 5e, g, 6d, e, Supplementary Fig. 7a, b, Supplementary Fig. 9a–d, h, i. For live cell imaging, the environment chamber was stabilized to 37 °C and $CO_2$ was provided by LCI FC-5N $CO_2$ mixer (Live Cell Instrument) and calibrated to maintain normal pH in cell culture media. For imaging heat stressed cells, the on-stage incubator (Live Cell Instrument CU-501) was heated to and stabilized at 42 °C. To avoid drifting, cells were pre-treated in a 42 °C $CO_2$ incubator for 15 min before they were transferred to the microscope and allowed 30 min to further stabilize before imaging starts.

### Correction of chromatic aberration, image analysis and statistics

Chromatic aberration of confocal images along the z direction was calibrated using 0.1 µm Tetraspec Microspheres (Thermo T7279) and corrected in ImageJ/Fiji[125] using a custom Jython script. 3D reconstruction and analysis of z-stacks were performed in Imaris whereas single z-slice images were analyzed using custom ImageJ Jython scripts. Measurements made in Imaris and ImageJ were analyzed using custom R scripts.

### Quantification of co-aggregates

For quantification of the (volume) percentage of SEC16A inclusions with TDP43 aggregation, TDP43/SEC16A coaggs and SEC16A inclusions without TDP43 were respectively identified in Imaris using its Labkit machine learning plugin[126]. For other quantifications, inclusions of two different proteins, e.g. SEC16A and $Hsp104^{DWB}$, were respectively identified in Imaris by manual thresholding based on local contrast, and the mutual overlap volumes between pairs of aggregates were measured. A SEC16A inclusion is categorized as in colocalization with $Hsp104^{DWB}$ if the overlap volume is no less than 80% of the former's volume.

### Fluorescence recovery after photobleaching (FRAP) assay

Aggregates were imaged for 11 frames before photobleaching by high power laser in part or in full. Then the aggregates were imaged continuously for at least 2.5 min and quantified in ImageJ using a custom Jython script.

### RNA inhibition (RNAi)

TriFECTa RNAi Kits including predesigned dicer-substrate small interference RNAs (DsiRNAs) were purchased from IDT. The sequences of DsiRNAs are listed in Supplementary Data 2. Each DsiRNA was co-transfected at a final concentration of 10 nM with plasmids using Lipofectamine 3000 according to the manufacturer's protocol. Briefly, DsiRNAs were immediately added after mixing Lipofectamine 3000 and P3000-bound plasmids.

### Generation of in-frame knock-in cell lines by CRISPR/Cas

mScarlet-I-G3BP1 in-frame tagging was conducted using Alt-R CRISPR/Cas system (IDT) according to the vendor's protocol with minor modifications. Briefly, a crRNA targeting the N-terminus of G3BP1 (synthesized at IDT, sequence available in Supplementary Data 2) was annealed with an equimolar amount of tracrRNA (IDT 1072534) to form the guide RNA (gRNA) duplex. Then the gRNA was mixed with *Sp*Cas9 (IDT 1081059) to form the gRNA/Cas9 complex, which in turn was co-transfected with a mScarlet-I donor (synthesized at IDT, sequence

available in Supplementary Data 2) into RPE-1 by the Neon Electroporation system (Thermo MPK1025). Cells expressing mScarlet-I-G3BP1 were sorted twice by fluorescence-activated cell sorting (FACS) on a Sony SH800S. PCR genotyping and WB showed that cells were heterozygous for mScarlet-I-G3BP1 tagging.

### Western blot (WB)

Cells cultured in each 35 mm dish were dissolved in 200-300 µL RIPA buffer (Thermo 89900) + 2 mM PMSF (Sigma P7626) + 3 µL Protease Inhibitor Cocktail (PIC, Sigma P8340) with regular swirling for 10 min. The protein concentrations of cell lysates were measured using BCA assay (Thermo 23225) and equal amounts of proteins were loaded onto 4-15 % polyacrylamide gradient gels (Bio-Rad 4561084) and fractionated by SDS-polyacrylamide gel electrophoresis (SDS-PAGE). Then proteins were electroblotted onto nitrocellulose membranes (BIO-RAD 1704158). After blocking in Odyssey Blocking Buffer (PBS, LI-COR 927), membranes were incubated sequentially with primary and secondary antibodies in Odyssey Blocking Buffer mixed with an equal volume of PBS + 0.2% [v/v] Tween 20. After each incubation, membranes were washed four times in PBST. Tween 20 was removed by rinsing in PBS before detecting the fluorescence of secondary antibodies using a LI-COR Odyssey CLx Scanner. The fluorescence of protein bands was quantified in ImageStudioLite (Bio-Rad).

### Aggregate purification

HEK293T cells cultured in two T225 flasks (Thermo 159934) were respectively transfected with plasmids carrying $Hsp104^{DWB}$-mEGFP-FLAG and, as a control, $Hsp104^{DWB}$-mEGFP. 24 hr after transfection, both flasks were transferred to a 42 °C $CO_2$ incubator for 12 hr to exacerbate protein aggregation. Then cells were gently washed once in PBS and harvested by washing off using PBS. The pellets from centrifugation at 120 g for 5 min was washed again using PBS and frozen in liquid nitrogen for future use. When needed, the frozen pellets were thawed at 4 °C, each lysed by incubation in 1000 µL RIPA buffer + 2 mM PMSF + 60 µL PIC + 112.5 Kunitz Unit/mL DNase I (RNase-free, NEB M0303) + 2.5 mM $MgCl_2$ (Sigma 5985-OP) with occasional pipette aspiration, and a brief centrifugation at 150 g for 5 min was conducted to remove cell debris. A small aliquot of the supernatant was used for BCA assay of protein concentration whereas the rest was loaded onto sucrose gradient layers of 20% and 50% [w/v] sucrose, each dissolved in 1500 µL RIPA buffer. Centrifugation at 60,000 *g* for 30 min on an ultracentrifuge (Thermo Sorvall WX100) enriched $Hsp104^{DWB}$-mEGFP(-FLAG)-labeled aggregates at the interface between 20 and 50% [w/v] sucrose. This layer was extracted through needle and syringe to yield ~750 µL of sample, which in turn was mixed with 200 µL of pre-equilibrated anti-FLAG M2 resin (Sigma A2220), rotated at 4 °C for 1 hr, and washed three times with RIPA buffer to immunoprecipitate $Hsp104^{DWB}$-mEGFP-FLAG-labeled aggregates. In the end, aggregates were eluted in urea elution buffer (8 M urea, 20 mM Tris pH=7.4, 100 mM NaCl). At each step, the presence of $Hsp104^{DWB}$-mEGFP-FLAG-labeled aggregates was checked by microscopy, and aliquots were saved for analysis by SDS-PAGE and Coomassie Brilliant Blue staining or WB.

### Liquid chromatography-tandem mass spectrometry (LC-MS/MS)

Proteins were reduced by 10 mM TCEP for 20 min at RT and alkylated with 55 mM 2-chloroacetamide (CAA) in the dark for 30 min. Then, the proteins were digested with 2 µg endoproteinase LysC for 3 hr followed by 2 µg trypsin at 37 °C overnight, and the digestion was terminated by adding trifluoroacetic acid (TFA) to a final concentration of 1% [v/v]. Subsequently, the peptides were desalted using C18 HLB cartridges (Waters), dried by centrifugal evaporation, and resuspended in 25 µl TEAB, pH = 8.5. The samples were differentially labeled with TMT10-plex isobaric tandem mass tags (Thermo) at 25 °C overnight, and the reaction was quenched by addition of 30 µl of 1 M ammonium formate, pH = 10 before pooling all samples into a low-binding microfuge tube. The pooled samples were desalted and fractionated on a self-packed spin column filled with C18 beads (Dr Maisch) in the step gradient of 14%, 24% and 60% [v/v] acetonitrile dissolved in 10 mM ammonium formate, pH=10. Each fraction was dried by centrifugal evaporation and further washed and dried twice by addition of 60% [v/v] acetonitrile + 0.1% [v/v] formic acid to remove residual ammonium formate. Then the samples were resuspended in 10 µl of 2% [v/v] acetonitrile + 0.06% [v/v] TFA + 0.5% [v/v] acetic acid and transferred to an autosampler plate. Online chromatography was performed using an EASY-nLC 1000 liquid chromatography system (Thermo) with a single-column setup and 0.1% [v/v] formic acid and 0.1% [v/v] formic acid + 99% [v/v] acetonitrile as mobile phases. The fractionated samples were injected and separated on an Easy-Spray reversed-phase C18 analytical column (Thermo) with 75 µm inner diameter, 50 cm length and 2 µm particle size. The column was maintained at 50 °C in 2–33% [v/v] acetonitrile gradient for over 55 min, followed by an increase to 45% [v/v] over the next 5 min, and then to 95% [v/v] over 5 min. The final mixture was maintained on the column for 4 min to elute all remaining peptides. The total run duration for each sample was 70 min at a constant flow rate of 300 nL/min. MS data were acquired on a Q Exactive HFX mass spectrometer (Thermo) using data-dependent mode. Samples were ionized under 2.1 kV and 300 °C at the nanospray source. Positively charged precursor signals (i.e. MS1) were detected using an Orbitrap analyzer set to a resolution of 60,000, automatic gain control (AGC) target of 3,000,000 ions, and max injection time (IT) of 50 ms. Precursors with charges 2–7 of the highest ion counts in each MS1 scan were further fragmented using higher-energy collision dissociation (HCD) at 36% normalized collision energy. The fragment signals (i.e. MS2) were analyzed by the Orbitrap analyzer at a resolution of 7500, AGC of 100,000 and max IT of 100 ms. Data-dependent (MS2) scans were acquired in Top40 mode. To avoid re-sampling of high abundance peptides, the precursors used for MS2 scans were excluded for 30 sec.

### Proteomics data analysis

Proteins were identified using Proteome Discoverer v2.3 (Thermo). Briefly, the raw mass spectra were searched against human primary protein sequences retrieved from Swiss-Prot (June 11 2019 release)[127] with carbamidomethylation on Cys and TMT10-plex on Lys and N-terminus set as fixed modifications, and deamidation of Asn and Gln, acetylation of N-terminus, and Met oxidation as dynamic modifications. Trypsin/P was set as the digestion enzyme and allowed up to three missed cleavage sites. Precursors and fragments of mass errors within 10 ppm and 0.8 Da, respectively, were accepted, while reporter ions were at least 1 Da apart from each other. Peptides were matched to the spectra at a false discovery rate (FDR) of 1% (strict) and 5% (relaxed) against the decoy database and quantitated using TMT10-plex method. The search results were further processed using a custom R script, in which Gene Ontology (GO) enrichment was performed using clusterProfiler[128,129]. The SG/nucleolus proteome, IDR-containing proteins and LLPS substrates were retrieved from previous publications and databases[130–133].

### Retention Using Selective Hooks (RUSH) assay for measuring ER-to-Golgi transport

RUSH was performed as previously described with minor modifications (Supplementary Fig. 8a)[79]. Briefly, the RPE-1 cell culture media was substituted with custom made biotin-free DMEM:F12 media (Cell Culture Technologies) + 10% [v/v] FBS from seeding (1 d before transfection). Then a plasmid carrying both the ER anchor ss-Strep-KDEL and the reporter ManII (aa1-116 only)-SBP-mCherry or TNFα-SBP-mCherry was co-transfected with TDP43 and SEC16A constructs using Lipofectamine 3000. To release cargo retention, D-biotin (Thermo

B20656) was added to a final concentration of 40 µM. For tracking ERES in timelapse imaging, SEC16A inclusions were identified in ImageJ using ilastik machine learning plugin[134] and then tracked by Trackmate[135]. The trajectories were analyzed by custom R scripts. Only SEC16A inclusions that enriched transport cargo (RUSH-TNFα) and tracked for no less than 10 frames (~15 sec) were used for cross-correlation (CC) analysis.

### AP21967-induced TDP43-ERES co-aggregation

3xFKBP-TDP43-mNG and 3xFRB*-Halo-SEC16A were co-transfected with the RUSH-TNFα construct. 1 µM rapamycin analog AP21967 (AP, Takara 635056) was added ~18 hr post-transfection to treat the cells for 6–10 hr to induce co-aggregation.

### Differentiation of motor neurons (MNs) from stem cells

The use of stem cells for MN differentiation was approved by the Human Biomedical Research Office, Agency for Science, Technology and Research of Singapore under protocol number 05-02-028. The human embryonic stem cells (hESCs) and induced pluripotent stem cells (hiPSCs) used in this study are: NDS00268, NDS00269 and NDS00270 (ALS patients) and BJ, GM23720 and H9 (non-ALS). BJ was obtained from National Center for Global Health (Japan), GM23720 was obtained from the NIGMS Human Genetic Cell Repository, H9 was purchased from Corning, and NDS00268, NDS00269, NDS00270 were obtained from NINDS Human Cell and Data Repository. The induction of MNs from stem cells were performed according to previous publications[136,137] and illustrated in Supplementary Fig. 10a. In brief, stem cells were cultured on Matrigel (Corning 354230)-coated plates in StemMACS iPS-Brew XF (Miltenyi Biotec 130-104-368). The cell culture media was changed every other day and cells were passaged at a split ratio between 1: 6 to 1: 10 every 6-8 days. On the day of differentiation (D0), stem cells were digested with Accutase (Nacalai Tesque 12679-54) for 5-10 min to acquire single-cell suspensions. Accutase was removed by centrifugation and PBS wash. Then cells were seeded at 70% confluency on dishes pre-coated with Matrigel and cultured in StemMACS iPS-Brew XF + 5 µM Y-27632 (STEMCELL Technologies 72304). On D1, the media was replaced with Neural Induction Media (NIM) comprising the Neural Media (NM) + 0.5 µM LDN193189 (STEMCELL Technologies 72147) + 4.25 µM CHIR99021 (Miltenyi Biotec 130106539), where NM is a mixture of 50% [v/v] DMEM:F12 + 50% [v/v] MACS Neuro Media (Miltenyi Biotec 130-093-570) + 0.5x GlutaMax (Thermo 35050061) + 1x NEAA (Thermo 11140050) + 1x N-2 (Thermo 17502048) + 1x MACS NeuroBrew-21 (Miltenyi Biotec 130-093-566). On D3, 1 µM retinoic acid (RA, Sigma R2625) was supplemented to the media, which was then changed every 2-3 days until D7 or when cells became confluent. At this point, stem cells have differentiated into MN progenitors, which can be passaged at a ratio between 1: 2 and 1: 3 onto new Matrigel-coated dishes. These progenitor cells were cultured in NIM + 1 µM RA + 5 µM Y-27632 and the media was changed every day. From D11, MN differentiation media, i.e. NM + 1 µM RA + 1 µM Purmorphamine (Miltenyi Biotec 130-104-465), was added and changed every other day until D17. Then MN maturation media, i.e. NM + 10 ng/mL GDNF (Miltenyi Biotec 130-129-547) + 10 ng/mL BDNF (Miltenyi Biotec 130-093-811) + 200 µM L-ascorbic acid (Sigma A5960), was added and changed every other day until MNs were ready on D28. The quality of MNs was checked by morphology and IF staining of (motor) neuron markers including NeuN/RBFOX3, NFM and ChAT.

### Immunofluorescence staining of post-mortem ALS patient samples

The post-mortem samples of ALS patients were acquired from the Johns Hopkins/Temple University ALS Postmortem Core in form of formalin-fixed paraffin-embedded (FFPE) tissue sections of approximately 20 mm×10 mm x 5 µm in dimensions. The demographic data of these patients are shown in Supplementary Data 3. For immunofluorescence staining, the samples were deparaffinized by incubating thrice in fresh Xylene (Sigma 534056) and rehydrated by incubating twice in ethanol and once in 90% and 70% [v/v] ethanol. Each incubation time is 5 min. Then the samples were boiled in epitope retrieval solution (IHC World IW-1100) in an autoclave (Hirayama HV-50) using the liquid cycle (121 °C 15 min), washed twice with PBS, and permeabilized for 10 min in PBS + 0.4% [v/v] Triton X-100. After three PBS washes, the samples were blocked in serum free protein block (Agilent X090930-2) for 1 hr at RT, and incubated with primary antibodies diluted in background reducing antibody diluent (Agilent S302283-2) overnight at RT. After three PBS washes, the samples were incubated with diluted secondary antibodies for 2 hr at RT and washed with PBS. The nuclei were stained by incubation with 1 µg/mL DAPI (Sigma MBD0015) in PBS for 30 min at RT followed by three more PBS washes. The stained sections were preserved in Prolong Gold antifade mountant (Thermo P36930) with coverslips sealed by transparent nail polish (Beauty Language). For image quantification, only cells positive for anti-NeuN immunostaining were counted. The analyzes of these patient samples were performed in a double-blinded manner.

### Reporting summary

Further information on research design is available in the Nature Portfolio Reporting Summary linked to this article.

## Data availability

MS proteomics data have been deposited to the Japan ProteOme STandard Repository (jPOSTrepo) as JPST002060. Source data are provided with this paper.

## References


1. Zeskind, B. J. et al. Nucleic acid and protein mass mapping by live-cell deep-ultraviolet microscopy. *Nat. Methods* **4**, 567–569 (2007).
2. Ellis, R. J. Macromolecular crowding: an important but neglected aspect of the intracellular environment. *Curr. Opin. Struct. Biol.* **11**, 114–119 (2001).
3. Uversky, V. N. Intrinsically disordered proteins in overcrowded milieu: membrane-less organelles, phase separation, and intrinsic disorder. *Curr. Opin. Struct. Biol.* **44**, 18–30 (2017).
4. Saad, S. & Jarosz, D. F. Protein self-assembly: A new frontier in cell signaling. *Curr. Opin. cell Biol.* **69**, 62–69 (2021).
5. Ellis, R. J. & Minton, A. P. Protein aggregation in crowded environments. *Biol. Chem.* **387**, 485–497 (2006).
6. Sontag, E. M., Samant, R. S. & Frydman, J. Mechanisms and functions of spatial protein quality control.*Annu. Rev. Biochem.* **86**, 97–122 (2017).
7. Hipp, M. S., Kasturi, P. & Hartl, F. U. The proteostasis network and its decline in ageing. *Nat. Rev. Mol. cell Biol.* **20**, 421–435 (2019).
8. Chiti, F. & Dobson, C. M. Protein misfolding, functional amyloid, and human disease. *Annu. Rev. Biochem.* **75**, 333–366 (2006).
9. Soto, C. & Pritzkow, S. Protein misfolding, aggregation, and conformational strains in neurodegenerative diseases. *Nat. Neurosci.* **21**, 1332–1340 (2018).
10. Neumann, M. et al. Ubiquitinated TDP-43 in frontotemporal lobar degeneration and amyotrophic lateral sclerosis. *Sci. (N. Y., NY)* **314**, 130–133 (2006).
11. Moda, F. et al. Secondary protein aggregates in neurodegenerative diseases: almost the rule rather than the exception. *Front Biosci. (Landmark Ed.)* **28**, 255 (2023).
12. Robinson, J. L. et al. Neurodegenerative disease concomitant proteinopathies are prevalent, age-related and APOE4-associated. *Brain* **141**, 2181–2193 (2018).
13. Alberti, S. et al. A user's guide for phase separation assays with purified proteins. *J. Mol. Biol.* **430**, 4806–4820 (2018).

14. Nilsson, M. R. Techniques to study amyloid fibril formation in vitro. *Methods* **34**, 151–160 (2004).
15. Mann, J. R. et al. RNA binding antagonizes neurotoxic phase transitions of TDP-43. *Neuron* **102**, 321–338.e328 (2019).
16. Mateju, D. et al. An aberrant phase transition of stress granules triggered by misfolded protein and prevented by chaperone function. *EMBO J.* **36**, 1669–1687 (2017).
17. Patel, A. et al. A liquid-to-solid phase transition of the ALS protein FUS accelerated by disease mutation. *Cell* **162**, 1066–1077 (2015).
18. Gleixner, A. M. et al. NUP62 localizes to ALS/FTLD pathological assemblies and contributes to TDP-43 insolubility. *Nat. Commun.* **13**, 3380 (2022).
19. Chou, C.-C. et al. TDP-43 pathology disrupts nuclear pore complexes and nucleocytoplasmic transport in ALS/FTD. *Nat. Neurosci.* **21**, 228–239 (2018).
20. Johnston, J. A., Ward, C. L. & Kopito, R. R. Aggresomes: a cellular response to misfolded proteins. *J. cell Biol.* **143**, 1883–1898 (1998).
21. Kopito, R. R. Aggresomes, inclusion bodies and protein aggregation. *Trends Cell Biol.* **10**, 524–530 (2000).
22. Weisberg, S. J. et al. Compartmentalization of superoxide dismutase 1 (SOD1G93A) aggregates determines their toxicity. *Proc. Natl Acad. Sci. USA* **109**, 15811–15816 (2012).
23. Ogrodnik, M. et al. Dynamic JUNQ inclusion bodies are asymmetrically inherited in mammalian cell lines through the asymmetric partitioning of vimentin. *Proc. Natl Acad. Sci. USA* **111**, 8049–8054 (2014).
24. Kon, T. et al. Accumulation of Nonfibrillar TDP-43 in the Rough Endoplasmic Reticulum Is the Early-Stage Pathology in Amyotrophic Lateral Sclerosis. *J. Neuropathol. Exp. Neurol.* **81**, 271–281 (2022).
25. Erjavec, N., Larsson, L., Grantham, J. & Nyström, T. Accelerated aging and failure to segregate damaged proteins in Sir2 mutants can be suppressed by overproducing the protein aggregation-remodeling factor Hsp104p. *Genes Dev.* **21**, 2410–2421 (2007).
26. Liu, B. et al. The polarisome is required for segregation and retrograde transport of protein aggregates. *Cell* **140**, 257–267 (2010).
27. Spokoini, R. et al. Confinement to organelle-associated inclusion structures mediates asymmetric inheritance of aggregated protein in budding yeast. *Cell Rep.* **2**, 738–747 (2012).
28. Zhou, C. et al. Motility and segregation of Hsp104-associated protein aggregates in budding yeast. *Cell* **147**, 1186–1196 (2011).
29. Grimminger-Marquardt, V. & Lashuel, H. A. Structure and function of the molecular chaperone Hsp104 from yeast. *Biopolymers* **93**, 252–276 (2010).
30. Harari, A., Zoltsman, G., Levin, T. & Rosenzweig, R. Hsp104 N-terminal domain interaction with substrates plays a regulatory role in protein disaggregation. *Febs j.* **289**, 5359–5377 (2022).
31. Yokom, A. L. et al. Spiral architecture of the Hsp104 disaggregase reveals the basis for polypeptide translocation. *Nat. Struct. Mol. Biol.* **23**, 830–837 (2016).
32. Gates, S. N. et al. Ratchet-like polypeptide translocation mechanism of the AAA+ disaggregase Hsp104. *Sci. (N. Y., NY)* **357**, 273–279 (2017).
33. Zhou, C. et al. Organelle-based aggregation and retention of damaged proteins in asymmetrically dividing Cells. *Cell* **159**, 530–542 (2014).
34. Shorter, J. The mammalian disaggregase machinery: Hsp110 synergizes with Hsp70 and Hsp40 to catalyze protein disaggregation and reactivation in a cell-free system. *PloS one* **6**, e26319 (2011).
35. Saha, I. et al. The AAA+ chaperone VCP disaggregates Tau fibrils and generates aggregate seeds in a cellular system. *Nat. Commun.* **14**, 560 (2023).
36. DeSantis, M. E. et al. Operational plasticity enables hsp104 to disaggregate diverse amyloid and nonamyloid clients. *Cell* **151**, 778–793 (2012).
37. Jackrel, M. E. et al. Potentiated Hsp104 variants antagonize diverse proteotoxic misfolding events. *Cell* **156**, 170–182 (2014).
38. Bösl, B., Grimminger, V. & Walter, S. Substrate binding to the molecular chaperone Hsp104 and its regulation by nucleotides. *J. Biol. Chem.* **280**, 38170–38176 (2005).
39. Bodnar, A. G. et al. Extension of life-span by introduction of telomerase into normal human cells. *Sci. (N. Y., NY)* **279**, 349–352 (1998).
40. Vabulas, R. M., Raychaudhuri, S., Hayer-Hartl, M. & Hartl, F. U. Protein folding in the cytoplasm and the heat shock response. *Cold Spring Harb. Perspect. Biol.* **2**, a004390 (2010).
41. Rzechorzek, N. M. et al. A daily temperature rhythm in the human brain predicts survival after brain injury. *Brain* **145**, 2031–2048 (2022).
42. Kawaguchi, Y. et al. The deacetylase HDAC6 regulates aggresome formation and cell viability in response to misfolded protein stress. *Cell* **115**, 727–738 (2003).
43. Gamerdinger, M., Kaya, A. M., Wolfrum, U., Clement, A. M. & Behl, C. BAG3 mediates chaperone-based aggresome-targeting and selective autophagy of misfolded proteins. *EMBO Rep.* **12**, 149–156 (2011).
44. Biel, T. G. et al. Mitochondrial dysfunction generates aggregates that resist lysosomal degradation in human breast cancer cells. *Cell Death Dis.* **11**, 460 (2020).
45. Graham, F. L., Smiley, J., Russell, W. C. & Nairn, R. Characteristics of a human cell line transformed by DNA from human adenovirus type 5. *J. Gen. Virol.* **36**, 59–74 (1977).
46. Geiger, T., Wehner, A., Schaab, C., Cox, J. & Mann, M. Comparative proteomic analysis of eleven common cell lines reveals ubiquitous but varying expression of most proteins. *Mol. Cell Proteom.* **11**, M111.014050 (2012).
47. Copin, R. et al. The monoclonal antibody combination REGEN-COV protects against SARS-CoV-2 mutational escape in preclinical and human studies. *Cell* **184**, 3949–3961. e3911 (2021).
48. Lin, Y., Protter, D. S., Rosen, M. K. & Parker, R. Formation and maturation of phase-separated liquid droplets by RNA-binding proteins. *Mol. cell* **60**, 208–219 (2015).
49. Harrison, A. F. & Shorter, J. RNA-binding proteins with prion-like domains in health and disease. *Biochemical J.* **474**, 1417–1438 (2017).
50. Strambio-De-Castillia, C., Niepel, M. & Rout, M. P. The nuclear pore complex: bridging nuclear transport and gene regulation. *Nat. Rev. Mol. Cell Biol.* **11**, 490–501 (2010).
51. Bastos, R., Pouplana, R., Enarson, L., Bodoor, M. & Burke, K. B. Nup84, a novel nucleoporin that is associated with CAN/Nup214 on the cytoplasmic face of the nuclear pore complex. *J. Cell Biol.* **137**, 989–1000 (1997).
52. Bernad, R., Engelsma, D., Sanderson, H., Pickersgill, H. & Fornerod, M. Nup214-Nup88 nucleoporin subcomplex is required for CRM1-mediated 60 S preribosomal nuclear export. *J. Biol. Chem.* **281**, 19378–19386 (2006).
53. Frottin, F. et al. The nucleolus functions as a phase-separated protein quality control compartment. *Sci. (N. Y., NY)* **365**, 342–347 (2019).
54. Watson, P., Townley, A. K., Koka, P., Palmer, K. J. & Stephens, D. J. Sec16 defines endoplasmic reticulum exit sites and is required for secretory cargo export in mammalian cells. *Traffic* **7**, 1678–1687 (2006).
55. Budnik, A. & Stephens, D. J. ER exit sites–localization and control of COPII vesicle formation. *FEBS Lett.* **583**, 3796–3803 (2009).

56. Weigel, A. V. et al. ER-to-Golgi protein delivery through an interwoven, tubular network extending from ER. *Cell* **184**, 2412–2429.e2416 (2021).
57. Gallo, R., Rai, A. K., McIntyre, A. B. R., Meyer, K. & Pelkmans, L. DYRK3 enables secretory trafficking by maintaining the liquid-like state of ER exit sites. *Dev. Cell* **58**, 1880–1897.e1811 (2023).
58. Beck, M. & Hurt, E. The nuclear pore complex: understanding its function through structural insight. *Nat. Rev. Mol. cell Biol.* **18**, 73–89 (2017).
59. Jain, S. et al. ATPase-modulated stress granules contain a diverse proteome and substructure. *Cell* **164**, 487–498 (2016).
60. Ding, Y. et al. Ratiometric biosensors based on dimerization-dependent fluorescent protein exchange. *Nat. Methods* **12**, 195–198 (2015).
61. Matsuki, H. et al. Both G3BP1 and G3BP2 contribute to stress granule formation. *Genes Cells: devoted Mol. Cell. mechanisms* **18**, 135–146 (2013).
62. Tourrière, H. et al. The RasGAP-associated endoribonuclease G3BP mediates stress granule assembly. *J. cell Biol.* **222**, e200212128072023new (2023).
63. Liu-Yesucevitz, L. et al. Tar DNA binding protein-43 (TDP-43) associates with stress granules: analysis of cultured cells and pathological brain tissue. *PloS one* **5**, e13250 (2010).
64. Dammer, E. B. et al. Coaggregation of RNA-binding proteins in a model of TDP-43 proteinopathy with selective RGG motif methylation and a role for RRM1 ubiquitination. *PloS one* **7**, e38658 (2012).
65. Zacharogianni, M., Aguilera-Gomez, A., Veenendaal, T., Smout, J. & Rabouille, C. A stress assembly that confers cell viability by preserving ERES components during amino-acid starvation. *eLife* **3**, e04132 (2014).
66. van Leeuwen, W. et al. Stress-induced phase separation of ERES components into Sec bodies precedes ER exit inhibition in mammalian cells. *J. Cell Sci.* **135**, jcs260294 (2022).
67. Kurokawa, K. & Nakano, A. The ER exit sites are specialized ER zones for the transport of cargo proteins from the ER to the Golgi apparatus. *J. Biochem* **165**, 109–114 (2019).
68. Saito, K., Maeda, M. & Katada, T. Regulation of the sar1 GTPase cycle is necessary for large cargo secretion from the endoplasmic reticulum. *Front Cell Dev. Biol.* **5**, 75 (2017).
69. Eck, R. J., Kraemer, B. C. & Liachko, N. F. Regulation of TDP-43 phosphorylation in aging and disease. *Geroscience* **43**, 1605–1614 (2021).
70. Brady, O. A., Meng, P., Zheng, Y., Mao, Y. & Hu, F. Regulation of TDP-43 aggregation by phosphorylation and p62/SQSTM1. *J. Neurochem* **116**, 248–259 (2011).
71. Li, H. Y., Yeh, P. A., Chiu, H. C., Tang, C. Y. & Tu, B. P. Hyperphosphorylation as a defense mechanism to reduce TDP-43 aggregation. *PloS one* **6**, e23075 (2011).
72. Hergesheimer, R. C. et al. The debated toxic role of aggregated TDP-43 in amyotrophic lateral sclerosis: a resolution in sight? *Brain* **142**, 1176–1194 (2019).
73. Nilaver, B. I. & Urbanski, H. F. Mechanisms underlying TDP-43 pathology and neurodegeneration: An updated Mini-Review. *Front Aging Neurosci.* **15**, 1142617 (2023).
74. Scotter, E. L. et al. Differential roles of the ubiquitin proteasome system and autophagy in the clearance of soluble and aggregated TDP-43 species. *J. Cell Sci.* **127**, 1263–1278 (2014).
75. Mackenzie, I. R. et al. Pathological TDP-43 distinguishes sporadic amyotrophic lateral sclerosis from amyotrophic lateral sclerosis with SOD1 mutations. *Ann. Neurol.* **61**, 427–434 (2007).
76. Zhang, Y. J. et al. Aberrant cleavage of TDP-43 enhances aggregation and cellular toxicity. *Proc. Natl Acad. Sci. USA* **106**, 7607–7612 (2009).
77. Düster, R., Kaltheuner, I. H., Schmitz, M. & Geyer, M. 1,6-Hexanediol, commonly used to dissolve liquid-liquid phase separated condensates, directly impairs kinase and phosphatase activities. *J. Biol. Chem.* **296**, 100260 (2021).
78. Wheeler, J. R., Matheny, T., Jain, S., Abrisch, R. & Parker, R. Distinct stages in stress granule assembly and disassembly. *eLife* **5**, e18413 (2016).
79. Boncompain, G. et al. Synchronization of secretory protein traffic in populations of cells. *Nat. Methods* **9**, 493–498 (2012).
80. Ilieva, E. V. et al. Oxidative and endoplasmic reticulum stress interplay in sporadic amyotrophic lateral sclerosis. *Brain* **130**, 3111–3123 (2007).
81. Oyanagi, K. et al. Spinal anterior horn cells in sporadic amyotrophic lateral sclerosis show ribosomal detachment from, and cisternal distention of the rough endoplasmic reticulum. *Neuropathol. Appl Neurobiol.* **34**, 650–658 (2008).
82. Matus, S., Valenzuela, V., Medinas, D. B. & Hetz, C. ER dysfunction and protein folding stress in ALS. *Int J. Cell Biol.* **2013**, 674751 (2013).
83. Medinas, D. B. et al. Endoplasmic reticulum stress leads to accumulation of wild-type SOD1 aggregates associated with sporadic amyotrophic lateral sclerosis. *Proc. Natl Acad. Sci. USA* **115**, 8209–8214 (2018).
84. Medinas, D. B., Cabral-Miranda, F. & Hetz, C. ER stress links aging to sporadic ALS. *Aging (Albany NY)* **11**, 5–6 (2019).
85. Nishitoh, H. et al. ALS-linked mutant SOD1 induces ER stress- and ASK1-dependent motor neuron death by targeting Derlin-1. *Genes Dev.* **22**, 1451–1464 (2008).
86. van Rheenen, W. et al. Common and rare variant association analyses in amyotrophic lateral sclerosis identify 15 risk loci with distinct genetic architectures and neuron-specific biology. *Nat. Genet.* **53**, 1636–1648 (2021).
87. Balendra, R. & Isaacs, A. M. C9orf72-mediated ALS and FTD: multiple pathways to disease. *Nat. Rev. Neurol.* **14**, 544–558 (2018).
88. Masrori, P. & Van Damme, P. Amyotrophic lateral sclerosis: a clinical review. *Eur. J. Neurol.* **27**, 1918–1929 (2020).
89. Suk, T. R. & Rousseaux, M. W. C. The role of TDP-43 mislocalization in amyotrophic lateral sclerosis. *Mol. Neurodegener.* **15**, 45 (2020).
90. Nover, L., Scharf, K. D. & Neumann, D. Cytoplasmic heat shock granules are formed from precursor particles and are associated with a specific set of mRNAs. *Mol. Cell. Biol.* **9**, 1298–1308 (1989).
91. Khong, A. et al. The stress granule transcriptome reveals principles of mrna accumulation in stress granules. *Mol. cell* **68**, 808–820.e805 (2017).
92. Hofmann, S., Kedersha, N., Anderson, P. & Ivanov, P. Molecular mechanisms of stress granule assembly and disassembly. *Biochimica et. Biophysica Acta (BBA) - Mol. Cell Res.* **1868**, 118876 (2021).
93. Reid, D. W. & Nicchitta, C. V. Primary role for endoplasmic reticulum-bound ribosomes in cellular translation identified by ribosome profiling. *J. Biol. Chem.* **287**, 5518–5527 (2012).
94. Jan, C. H., Williams, C. C. & Weissman, J. S. Principles of ER cotranslational translocation revealed by proximity-specific ribosome profiling. *Sci. (N. Y., NY)* **346**, 1257521 (2014).
95. Lim, L., Wei, Y., Lu, Y. & Song, J. ALS-causing mutations significantly perturb the self-assembly and interaction with nucleic acid of the intrinsically disordered prion-like domain of TDP-43. *PLoS Biol.* **14**, e1002338 (2016).
96. Scott, Z. C. et al. Endoplasmic reticulum network heterogeneity guides diffusive transport and kinetics. *Biophysical J.* **122**, 3191–3205 (2023).
97. Prasad, A., Bharathi, V., Sivalingam, V., Girdhar, A. & Patel, B. K. Molecular mechanisms of TDP-43 misfolding and pathology in amyotrophic lateral sclerosis. *Front Mol. Neurosci.* **12**, 25 (2019).
98. Vabulas, R. M. & Hartl, F. U. Protein synthesis upon acute nutrient restriction relies on proteasome function. *Sci. (N. Y., NY)* **310**, 1960–1963 (2005).

99. Medicherla, B. & Goldberg, A. L. Heat shock and oxygen radicals stimulate ubiquitin-dependent degradation mainly of newly synthesized proteins. *J. Cell Biol.* **182**, 663–673 (2008).
100. Kutay, U., Jühlen, R. & Antonin, W. Mitotic disassembly and reassembly of nuclear pore complexes. *Trends Cell Biol.* **31**, 1019–1033 (2021).
101. Thomas, L., Taleb Ismail, B., Askjaer, P. & Seydoux, G. Nucleoporin foci are stress-sensitive condensates dispensable for C. elegans nuclear pore assembly. *EMBO J.* **42**, e112987 (2023).
102. Soto, C. Unfolding the role of protein misfolding in neurodegenerative diseases. *Nat. Rev. Neurosci.* **4**, 49–60 (2003).
103. Kayatekin, C. et al. Prion-like proteins sequester and suppress the toxicity of huntingtin exon 1. *Proc. Natl Acad. Sci. USA* **111**, 12085–12090 (2014).
104. Bolognesi, B. et al. The mutational landscape of a prion-like domain. *Nat. Commun.* **10**, 4162 (2019).
105. Bence, N. F., Sampat, R. M. & Kopito, R. R. Impairment of the ubiquitin-proteasome system by protein aggregation. *Sci. (N. Y., NY)* **292**, 1552–1555 (2001).
106. Park, S. H. et al. PolyQ proteins interfere with nuclear degradation of cytosolic proteins by sequestering the Sis1p chaperone. *Cell* **154**, 134–145 (2013).
107. Garcia, D. M. et al. A prion accelerates proliferation at the expense of lifespan. *eLife* **10**, e60917 (2021).
108. Zappa, F. et al. The TRAPP complex mediates secretion arrest induced by stress granule assembly. *EMBO J.* **38**, e101704 (2019).
109. Yuan, F. et al. Membrane bending by protein phase separation. *Proc. Natl Acad. Sci. USA* **118**, e2017435118 (2021).
110. Mangiarotti A., Chen N., Zhao Z., Lipowsky R. & Dimova R. Membrane wetting, molding and reticulation by protein condensates. *bioRxiv*, 2022.2006.2003.494704 (2022).
111. Wang, X. et al. Manganese regulation of COPII condensation controls circulating lipid homeostasis. *Nat. cell Biol.* **25**, 1650–1663 (2023).
112. Cykowski, M. D. et al. Clinical significance of TDP-43 neuropathology in amyotrophic lateral sclerosis. *J. Neuropathol. Exp. Neurol.* **76**, 402–413 (2017).
113. Arseni, D. et al. Structure of pathological TDP-43 filaments from ALS with FTLD. *Nature* **601**, 139–143 (2022).
114. Hasegawa, M. et al. Phosphorylated TDP-43 in frontotemporal lobar degeneration and amyotrophic lateral sclerosis. *Ann. Neurol.* **64**, 60–70 (2008).
115. McGurk, L. et al. Poly-A binding protein-1 localization to a subset of TDP-43 inclusions in amyotrophic lateral sclerosis occurs more frequently in patients harboring an expansion in C9orf72. *J. Neuropathol. Exp. Neurol.* **73**, 837–845 (2014).
116. Wang, J. et al. Single-cell RNA-seq reveals early heterogeneity during aging in yeast. *Aging cell* **21**, e13712 (2022).
117. Consortium, T. T. M. A single-cell transcriptomic atlas characterizes ageing tissues in the mouse. *Nature* **583**, 590–595 (2020).
118. Simon, N. G. et al. Quantifying disease progression in amyotrophic lateral sclerosis. *Ann. Neurol.* **76**, 643–657 (2014).
119. Chiò, A. et al. Prognostic factors in ALS: a critical review. *Amyotroph. Lateral Scler.* **10**, 310–323 (2009).
120. Meneses, A. et al. TDP-43 pathology in Alzheimer's disease. *Mol. Neurodegener.* **16**, 84 (2021).
121. Zhang, S. et al. Genome-wide identification of the genetic basis of amyotrophic lateral sclerosis. *Neuron* **110**, 992–1008.e1011 (2022).
122. Shi, Y. et al. Haploinsufficiency leads to neurodegeneration in C9ORF72 ALS/FTD human induced motor neurons. *Nat. Med.* **24**, 313–325 (2018).
123. Soo, K. Y. et al. Rab1-dependent ER-Golgi transport dysfunction is a common pathogenic mechanism in SOD1, TDP-43 and FUS-associated ALS. *Acta Neuropathol.* **130**, 679–697 (2015).
124. Halloran, M. et al. Amyotrophic lateral sclerosis-linked UBQLN2 mutants inhibit endoplasmic reticulum to Golgi transport, leading to Golgi fragmentation and ER stress. *Cell. Mol. life Sci.: CMLS* **77**, 3859–3873 (2020).
125. Schindelin, J. et al. Fiji: an open-source platform for biological-image analysis. *Nat. Methods* **9**, 676–682 (2012).
126. Arzt, M. et al. LABKIT: Labeling and Segmentation Toolkit for Big Image Data. *Front. Comput. Sci.* **4**, 1–12 (2022).
127. Boutet, E., Lieberherr, D., Tognolli, M., Schneider, M. & Bairoch, A. *UniProtKB/Swiss-Prot. Methods Mol. Biol. (Clifton, NJ)* **406**, 89–112 (2007).
128. Consortium TGO. Gene Ontology Consortium: going forward. *Nucleic acids Res* **43**, D1049–D1056 (2015).
129. Yu, G., Wang, L. G., Han, Y. & He, Q. Y. clusterProfiler: an R package for comparing biological themes among gene clusters. *Omics* **16**, 284–287 (2012).
130. Marmor-Kollet, H. et al. Spatiotemporal proteomic analysis of stress granule disassembly using APEX reveals regulation by SUMOylation and links to ALS pathogenesis. *Mol. cell* **80**, 876–891.e876 (2020).
131. Thul, P. J. et al. A subcellular map of the human proteome. *Sci. (N. Y., NY)* **356**, eaal3321 (2017).
132. Piovesan, D. et al. MobiDB: intrinsically disordered proteins in 2021. *Nucleic acids Res.* **49**, D361–d367 (2021).
133. Wang, X. et al. LLPSDB v2.0: an updated database of proteins undergoing liquid-liquid phase separation in vitro. *Bioinforma. (Oxf., Engl.)* **38**, 2010–2014 (2022).
134. Berg, S. et al. ilastik: interactive machine learning for (bio)image analysis. *Nat. Methods* **16**, 1226–1232 (2019).
135. Ershov, D. et al. TrackMate 7: integrating state-of-the-art segmentation algorithms into tracking pipelines. *Nat. Methods* **19**, 829–832 (2022).
136. Hor, J. H. et al. Cell cycle inhibitors protect motor neurons in an organoid model of Spinal Muscular Atrophy. *Cell Death Dis.* **9**, 1100 (2018).
137. Hor, J. H. et al. ALS motor neurons exhibit hallmark metabolic defects that are rescued by SIRT3 activation. *Cell Death Differ.* **28**, 1379–1397 (2021).


## Acknowledgements

The authors would like to thank J. Shorter (UPenn) for recommending the DWB mutations for stable Hsp104-aggregate binding and generously sharing a $Hsp104^{DWB}$ construct. The authors thank P. Kanchanawong and K. Paramasivam for kindly sharing FP constructs, and B.C. Low for kindly sharing HEK293T cell line. The authors thank H.T. Ong and J.F.L. Chin from MBI Microscopy core, Singapore Microscopy and Bioimage Analysis (SIMBA), for help in correction of chromatic aberration in confocal imaging, and MBI Wet Lab Core for providing essential lab equipment. The authors are grateful to G. Thibault (NTU), B. Burke (A*STAR), T. Hiraiwa, G. Jedd (TLL), P.T. Matsudaira, J. Hu, M. Yao, W. Huang, L. Ruan (JHU), H. Wang, R. Das, T. Chew, Y. Tee, M. Pan, S. Ramachandran (JHU), B. S. Wong, X. Lan, K. Seah and Y. Lee for constructive discussions. This work was supported by R. Li's startup grant (A-0007081-00-00), a Tier 3 grant (A-0006324-03-00) received from Singapore Ministry of Education, a Mid-sized Grant (NRF-MSG-2023-0001) from Singapore National Research Foundation, and by the A*STAR core funding and Singapore National Research Foundation (under its NRF-SIS "SingMass" scheme) endowed to R.M. Sobota and L.C. Wang. H. W. would like to specially thank those who have maintained faith in him during difficult times.

## Author contributions

H.W. and R.L. designed the study and wrote the manuscript. H.W. conducted and performed data analysis for most experiments. L.C.W. performed LC-MS/MS. B.M.S. determined the dynamic/non-dynamic (solid/liquid-like) states of aggregates. D.L. derived MNs from stem cells. J.Z.

designed CRISPR/Cas for in-frame gene tagging. K.M.G. and K.W. prepared post-mortem tissue sections from ALS patient samples and helped optimize immunofluorescence staining protocol. R.G. assisted with molecular cloning and cell staining. C.J.J.Y., R.M.S. and L.W.O. contributed to experiment designs. R.L. supervised the project.

## Competing interests
The authors declare no competing interests.

## Additional information
**Supplementary information** The online version contains supplementary material available at https://doi.org/10.1038/s41467-024-52706-7.

**Correspondence** and requests for materials should be addressed to Rong Li.

**Peer review information** *Nature Communications* thanks Xiaowei Chen, Gunther Kahlert and the other, anonymous, reviewer(s) for their contribution to the peer review of this work. A peer review file is available.